Ultra-narrowband Metamaterial Absorbers for Multispectral Infrared Microsystems

A Thesis Presented

by

Sungho Kang

to

The Department of Electrical and Computer Engineering

in partial fulfillment of the requirements

for the degree of

Master of Science

in

Electrical and Computer Engineering

Northeastern University

Boston, Massachusetts

December 2018

Contents

List of Figures

List of Tables

List of Acronyms

AlN aluminum nitride

CMOS complementary metal oxide semiconductor

CST Computer Simulation Technology

EM electromagnetic

FTIR Fourier transform infrared

FWHM full-width at half-maximum

IPA isopropyl alcohol

IR infrared

LOR lift off resist

LWIR long wave infrared

MEMS micro-electro-mechanical systems

MIBK methyl isobutyl ketone

MIM metal-insulator-metal

MWIR mid-wavelength infrared

N/MEMS nano/micro electromechanical systems

NIR near infrared

OMS optically-actuated micromechanical switch

PMMA poly(methyl methacrylate)

RF radio frequency

SP surface plasmon

SEM scanning electron microscopy

SWIR short wavelength infrared

TE transverse electric

THz teraherz

TM transver magnetic

TMAH tetramethylammonium hydroxide

Abstract of the Thesis

Ultra-narrowband Metamaterial Absorbers for Multispectral Infrared Microsystems

by

Sungho Kang

Master of Science in Electrical and Computer Engineering

Northeastern University, December 2018

Dr. Matteo Rinaldi, Advisor

IR absorption spectroscopy is a powerful technique to identify and study chemicals or objects of various kinds in a non-disruptive way. Recently, the demand for high performance and compact IR spectroscopy systems has been steadily growing due to the advent of Internet of Things and the burgeoning development of miniaturized sensors. The key challenge lies in realizing multispectral absorber arrays that are lithographically defined and integrated on the same chip, with a minimized footprint. This challenge has been tackled in the study of metamaterials absorbers, the artificial materials composed of an array of subwavelength structures that manipulate electromagnetic waves to achieve extraordinary light absorption properties. The MIM IR absorbers, in particular, are characterized by the near-unity absorptance with lithographically tunable peak absorption wavelength and spectral selectivity in an ultra-thin form factor, suitable for the implementation of miniaturized spectroscopic IR microsystems. Nevertheless, there has been no accurate analytical model to guide the design of MIM IR absorbers with ultra-narrow absorption bandwidth and near-unity absorption, while meeting all the stringent requirements for high-resolution multispectral IR microsystems.

This thesis presents the modeling and characterization of ultra-narrowband MIM IR absorbers based on the modified circuit model capable of accurately predicting the spectral responses of MIM IR absorbers. The simultaneous excitation of electric and magnetic resonances in the MIM IR absorbers is modeled via the addition of coupling capacitance to the existing RLC circuit branch, resulting in the accurate description of the effective surface impedance. The model is experimentally validated in the mid-wavelength IR spectral range ($\lambda = 3 \sim 7\mu m$) and exploited for the first demonstration of a narrowband MIM IR absorber that exhibits performance approaching the predicted physical limits: full-width at half-maximum $\approx$3 % and near-unity absorption ($\eta > 99.7\%$) at 5.83 μm wavelength, while independent of incident angle and polarization of the impinging IR

radiation. Furthermore, the two novel plasmonically-enhanced IR microsystems, enabled by the high performance MIM IR absorbers, are also presented: multispectral resonant IR detectors and zero-power micromechanical photoswitches. The optimized ultra-narrowband MIM IR absorbers are proven to be the ideal candidates for the implementation of such new class of multispectral IR microsystems with the unprecedented performance beyond what the existing technologies can achieve.

Chapter 1

Introduction

Electromagnetic (EM) wave absorbers refer to the materials that convert the incident EM waves into different forms of energy such as heat or electrical currents. In other words, they suppress reflection, transmission and scattering of the incident waves while maximizing the absorption within the absorber by means of high intrinsic loss or proper engineering of optical properties. Depending on the region of EM spectrum in which the peak spectral absorption band is located, EM absorbers can be categorized accordingly into different regions of operating wavelengths. The earlier development of EM absorbers have been mostly focused in the RF regime ($3kHz \sim 300GHz$), due to the large demand in the applications such as communications and military defense. THz absorbers operate in a higher frequency regime ($0.3 \sim 3THz$) and are actively employed in the medical applications such as non-invasive alternative to X-ray imaging as well as in the homeland security applications where THz waves are used to deect concealed weapons underneath garments. In visible regime, camouflage technology based on cloaking devices and visible EM absorbers is an exciting research of interests to many scientists.

This thesis mainly focuses on the applications and the current state of technologies operating in the IR regime. IR radiation ($0.3 \sim 400THz$) absorbers have a very broad application field including thermal imaging, chemical spectroscopy, and energy harvesting. Due to the wide spectrum of IR regime, design of an IR absorber is very application-specific depending on the spectral region of operation. In this thesis, specific kinds of IR absorbers known as metal-insulator-metal IR absorbers are discussed in depth. The proposed absorbers are capable of absorbing MWIR waves with a very high spectral resolution and near-unity absorption. The applications of minaturized IR spectroscopy and zero-power micromechanical IR digitzers enabled by the unique absorption properties of MIM IR absorbers are also presented. In Chapter 1, introduction and background of

metamaterial infrared absorbers are presented. Next, design and optimization of MIM metamaterial IR absorbers are presented in Chapter 2. In Chapter 3 the two novel IR microsystems with integrated MIM IR absorbers are presented: multispectral resonant IR detectors and zero-power IR digitizers based on micromechanical photoswitches. Lastly in Chapter 4, conclusions and discussions of the impact and outlook of the proposed devices are presented.

1.1 Infrared Absorbers

IR absorbers can be categorized into different types based on their working wavelengths, bandwidths, or absorption physics. The brand spectrum of wavelengths in IR regime is subdivided into several regions and a variety of application exists in each spectrum range. The SWIR regime ($\lambda \approx 0.8 - 1.5\mu m$) is closest to the visible spectrum and therefore has the shortest IR wavelengths. Free space optical communications take advantage of the near infrared waves, due to the low attenuation in waveguides such as fiber optics. Energy harvesting is also a widely-explored application which captures the available EM energy such as from the sunlight, whose peak emission is in the NIR SWfIR regime, to generate useful electrical energy. The MWIR ($\lambda \approx 2 - 8\mu m$) and LWIR ($\lambda \approx 8 - 20\mu m$) are widely exploited for gas spectroscopy and thermal imaging. The MWIR and LWIR regions are also known as the chemical fingerprint regions where chemical IR spectroscopy take advatange of the strong absorption and emission peaks due to the molecular level rotational and vibrational resonance modes of various chemicals. Thermal imaging exploits the EM radiation from warm objects whose peak EM emission is located in LWIR regime.

IR absorbers can be further categorized based upon the physical mechanism of the IR absorption. Bulk IR absorbers are typically single-stack material IR absorbers that exploit the intrinsic loss properties. For instance, many dielectric materials exhibit high LWIR absorption due to the lattice phonon vibrations in LWIR regime (e.g., SiO_2, VO_x, or Si_3N_4). They are typically characterized by thickness-dependent absorption properties and broad absorption bandwidth, which are useful when a large amount of energy needs to be absorbed (e.g., energy harvesting) or the characteristic IR signature is inherently broadband (e.g., thermal imaging). On the other hand, engineered absorbers, such as Dallenbach or Salisbury absorber, can be classified as resonant absorbers since they are designed to resonate at a particular wavelength of interests and enhance absorption significantly in that specific spectral band [1, 2]. In particular, plasmonic and metamaterial absorbers whose effective surface impedance is artificially engineerd to match the impedance of free space have been recently developed thanks to the recent advancement in micro- and nano- fabrication techniques to realize

sub-wavelength scaled structures. Such IR absorbers typically exhibit nearly perfect absorption efficiency with narrow absorption bandwidths while maintainig the ultra-compact form factor. The advancement of such unique plasmonically-enhanced IR absorbers have opened up a new class of applications and is discussed in detail in the following sections.

1.2 Metamaterials

The field of metamaterials is a research area focusing on developing materials with extraordinary optical characteristics that are not found in nature by tailoring the effective electric and magnetic response of engineered materials. These materials consist of carefully-designed patterns that are usually arranged in a periodic manner much smaller than its working wavelength. The properties of the metamaterials can be tailored precisely to control the impinging electromagnetic waves in different ways such as steering, redirecting, focusing, absorbing, and reflecting. Such precise control of EM waves have been demonstrated for EM clocking, perfect absorbers, energy harvesting, and imaging beyond diffraction limit. Negative refractive index metamaterials, also known as left-handed metamaterials, is one of the most well-known examples of metamaterials which take advantage of artificial electric and magnetic resonance (electric permittivity, $\varepsilon < 0$, and magnetic permeability, $\mu < 0$, respectively) to realize a negative refractive index [3, 4]. Such discovery resulted in a new class of applications such as flat lens, invisibility, and beyond-diffraction imaging. Another type of metamaterials are high impedance surfaces, consisting of layers of metal and dielectric thin films whose geometric shapes and dimensions are precisely controlled to exhibit desired properties such as phase shifting and frequency selective responses. [5]. In particular, when the effective surface impedance of a high impedance surface matches to the free space impedance, one can achieve perfect absorption at the specfic wavelength [6]. These metamaterials are commonly referred to as metamaterial perfect absorbers, and have been demonstrated in a wide electromagnetic spectrum range from microwaves to optical regime.

1.3 Metamaterial Electromagnetic Absorbers

Electromagnetic perfect absorbers, in particular, have been investigated for a long time, for various applications including wireless communications, thermal emitters, sensors, photodetectors and photovoltaic structures. In an electromagnetic absorber, reflected and transmissited power are minimized, and for most cases, the incident light turns into heat, which could also be further used

to harvest energy in another energy domain. Unlike other metamaterial-enabled devices where losses are generally to be avoided, metamaterial absorbers take advantage of such loss, which mainly arises from a finite resistivity of metal or dielectric loss in the system. The metamaterial absorbers, if designed properly, can be applied in almost all electromagnetic regime, including radio frequency (RF) and microwave [7–9], THz [10–14], infrared [15–18], and visible [19–21]. Although many metamaterial-enabled EM absorbers are characterized by near-perfect absorption, there exist criteria that need to be considered when designing application-specific metamaterial absorbers, such as bandwidth, angular acceptance, and polarization sensitivity.

1.3.1 Working Frequency Bands

As mentioned above, metamaterial absorbers of diverse kinds have been explored to achieve high absorption in wide electromagnetic spectrum from RF to visible. One of the differences when designing metamaterial absorbers at different frequency regimes is the origin of loss that dominates the absoprtion. For instance, the eariler demonstration of metamaterial absorbers exploits dielectric loss associated in the split ring resonators and a cut wire separated by a dielectric layer to achieve 88% absorption at 11.5 GHz [22]. On the other hand, at higher frequency regime, Ohmic loss from metal layers start to dominate. While the microwave absorbers are mainly used in RF wireless communication applications [23], the higher frequency regime in THz, IR, and visible range can be useful for imaging and sensing applications. Since the size of the metamaterial structures are largely dependent on the operation wavelengths, the fabrication techniques also depend on the working spectral range. For instance, standard optical lithography techniques on a printed circuit board or a wafer-level substate can be used for metamamaterilas in low frequency regime, as the critical dimension of the standard optical lithography is much smaller in micro and nanometer scale. However, this prevents the use of conventional photolithography techniques to fabricate electromagnetic absorbers in higher frequency regime such as IR or visible. Recently, the advacement of nanofabrication techniques such as electron beam lithography and nano-imprinting techniques allow for the fabrication of sub-micron scale metamaterial absorbers in IR [17, 24–29] and visible [30] regimes.

1.3.2 Angle and Polarization Stability

Depending on the applications, angular response and polarization sensitivity are important characteristics of a metamaterial absorber. Metamaterial absorbers based on de-localized plasmons,

for instance, can be used for sensing applications and are typically characterized by small acceptance angle and polarization dependent absorption. On the other hand, wide acceptance angle and polarization insensitivity can be used to greatly enhance the absorption efficiency. In fact, both the acceptance angle and polarization sensitivity of the absorbers play a significant role in maximizing the total absorption, especially for non-invasive standoff chemical sensing applications, where the chemical compounds are inherently spread over a wide field of view with arbitrary orientations of molecular structures, resulting in random incident angles and polarizations.

1.3.3 Bandwidth

The bandwidth requirements for metamaterial absorber are also largely dependent on the applications. In the fields of photovoltaic devices such as thin film solar cells or thermo-photovoltaic systems, broadband absorption is preferred and the typical way of implementation to efficiently harvest available energy [31]. Solar cells, which take advantage of surrounding electromagnetic energy that is mostly available in visible spectrum prefer wide-angle polarization independent electromagnetic absorbers with wide bandwidth spanning as wide spectrum as possible [32]. On the other hand, for the applications of multi-spectral imaging or chemical sensing where spectral contents become of an important information, narrower absorption bandwidths become particularly important. In fact, many metamaterial absorbers that rely on the electromagnetic resonance inside the system exhibit narrow absorption bandwidths. The achievement of high absorptance in a narrow spectral band is particularly important for IR spectroscopy, since multiple chemical species may exhibit strongly confined spectral emission/absorption bands closely located to each other (e.g., $\lambda_0 = 4.25\mu m, 4.5\mu m$, for carbon dioxide and nitrous oxide, respectively).

1.3.4 Device Fabrication and Integration

Although conventional printed circuit board fabrication methods can be used to fabricate metamaterial absorbers for relatively low frequency such as in RF wireless communication systems, special techniques are required for shorter wavelength regime, such as THz, infrared, or visible frequencies. This is due to the inherent scaling of the metamaterial structures proportional to the wavelengths of operation. In other words, the metamaterial absorbers in higher frequency may require patterning of sub-micron nanostructures whose critical dimensions are much smaller than what the conventional photolithography techniques can achieve. Yet, the recent advancement of micro and nanofabrication techniques including electron-beam lithography and thin film deposition have

allowed for a reliable and repeatable production of sub-wavelength features. Furthremore, due to the compatibility with micro and nano fabrication techniques and the inherently small sub-wavelength form factor guarantee the semaless integration with the existing photonic microsystems.

1.4 Metamaterial Infrared Absorbers

Metamaterial IR absorbers, in particular, have allowed for the miniaturization of the conventional IR-enabled devices thanks to the ultra-thin form factor and compatibility with standard micro and nano fabrication techniques. Furthermore, the lithographically defined peak absorption wavelengths and narrow absorption bandwidths are the ideal characteristics for realiznig multispectral absorber arrays that are monolithically integrated on the same chip. A number of recently proposed metamaterial IR absorbers exploit strong surface plasmon (SP) resonances at metal-dielectric interfaces to demonstrate distinctively narrow absorption bands suitable for high spectral resolution spectroscopic applications, while maintaining high absorptance and lithographically tunable spectral absorption bands in a subwavelength form factor [33–39]. Nevertheless, many of the aforementioned devices rely on the excitation of de-localized SPs, which are inherently dependent on a fixed acceptance angle and dependence on polarization. Such constraints significantly lower total absorption compared to the bulk material counterpart, making them unable to meet all the stringent requirements suitable for miniaturized multispectral IR systems. On the otherhand, the localized surface plasmon absorption allows for 2-dimensional plasmon excitation and the design of four-fold symmetrical nanostructures, which translate into wider acceptance angle and polarization insensitivity, which increase absorption efficiency overall. The most common type of metamaterial IR absorbers enabled by localized plasmons is metal-insulator-metal (MIM) IR absorbers which can efficiently couple to the incident IR radiation via strong electric and magnetic resonances inside the cavity. Indeed, the MIM IR nanostructured absorbers are characterized by lithographically controlled tunability of the absorption wavelength and near-unity absorption with litttle contraints on angle or polarization [40–45]. In this context, the MIM IR absorbers are the ideal candidates for the implementation of compact IR spectroscopic microsystems. In this thesis, the design and characterization of MIM IR absorbers are discussed in detail in Chapter 2 and Chapter 3.

Chapter 2

Design of Metal-Insulator-Metal Infrared Absorbers

The MIM IR absorbers have been studied and employed in a variety of applications due to their unique characteristics of lithographically-controlled absorption wavelengths and near-unity absorption with little constraints on angle and polarization [46–51]. MIM IR absorbers adopt a similar structural configuration as the artificial metamaterial with magnetic response reported by Zhang et al., in that they both consist of an array of two parallel layers of metallic structures separated by a thin dielectric gap [52], which induces the effective electric and magnetic responses that are different from the bulk-state materials. Differently from [52], one of the metallic layers in MIM IR absorbers is an un-patterned optically thick continuous plane, which suppresses any transmitted power of incident IR. MIM IR absorbers achieve the near-unity absorption via a finite loss associated with the 2-D localized SPs excited in the tri-layer geometry consisting of an array of plasmonic nanostructure and the ground metal layer separated by a subwavelength thick dielectric spacer (Figure 2.1). Furthermore, the strong 2-D plasmon excitation of 4-fold symmetric nanostructures ensure a response with minimal constraints on the property of incident IR waves (i.e., angle and polarization), while maintaining spectral selective near-unity absorption [53]. Surely enough, these characteristics have made these absorbers the ideal candidates for a new class of plasmonically-enhanced IR sensing microsystems, such as spectrally selective microbolometers, nano/micro- electromechnical (N/MEMS) resonance IR sensors, solar cells [46], refractive index sensors [54–56], thermal sensors [51, 57, 58], surface-enhanced spectroscopy [59], and optically-actuated micromechanical photoswitches [47, 48].

Nevertheless, there has been no experimental realization of ultra-narrowband MIM IR

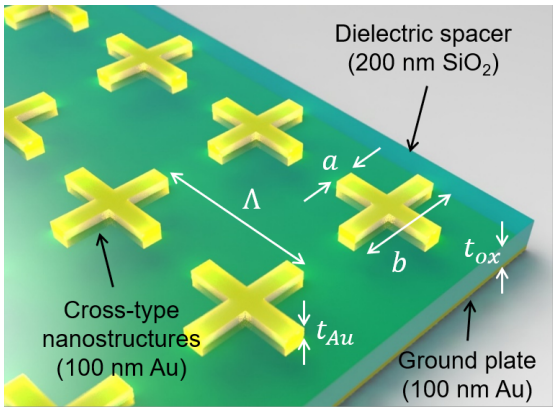

Figure 2.1: Schematic of MIM IR absorbers with cross-type nanostructures. The inset shows a cross-section of the MIM IR absorber highlighting the try-layer material stack.

absorbers specifically tailored for high resolution multispectral IR spectroscopy. In fact, early reports have shown full-width at half-maximum (FWHM) only as narrow as $\sim 15\%$ using MIM IR absorbers with suitably shaped nanostructures (e.g., square or circularly patches, holes, or crosses), which fall short from the required spectral resolution for IR spectroscopy [41, 44, 60]. This limitation is attributed to the absence of analytical tools that capture the physics of the system with respect to the parameters defined by the constituent materials and geometry.

Although a recent report by Lochbaum et al. highligths a narrower FHWM ($< 5\%$), such performance increase was not guided by a generalized analytical design method that directly relates absorption properties to the characteristic parameters (i.e., geometric dimensions and materials) of MIM IR absorbers, which is particularly important when designing an absorber with specific process constraints, such as lithography limits or material compatibility [26, 61]. In fact, many analytical models reported to date fail to investigate absorption, spectral bandwidths, and resonant wavelengths of the MIM IR absorbers in a concise and accurate form [28, 41, 43, 62–65]. In this chapter, a modified lumped equivalent circuit model for MIM IR absorbers is presented. The proposed analytical model can be used to investigate absorption, spectral bandwidths, and peak absorption wavelengths simultaneously in a concise form of spectral absorption response that could dramatically enhance the design and understanding of MIM IR absorbers.

2.1 Metal-insulator-metal IR Absorbers for Spectroscopic IR Sensing

The MIM IR absorbers consist of an array of subwavelength nanostructures and a continuous ground plane separated by a thin dielectric spacer. Although the nanostructures in the thesis are chosen to be 4-fold symmetric cross-shaped structures for polarization insensitivity and better field confinement, other arbitrary structures such as square and circular patches have been demonstrated in the past. The thickness of the continuous ground plane, placed a subwavelength gap away from the nanostructure array, is set to be optically thick so that the transmitted power is suppressed while sustaining the plasmonic resonance in the absorber. When the electromagnetic waves in a specific spectral band impinge on the absorber, the electric dipole resonance is excited by the array of nanostructures, inducing an antiparallel current in the ground layer via plasmonic coupling within the subwavelength dielectric gap (Figure 2.2).

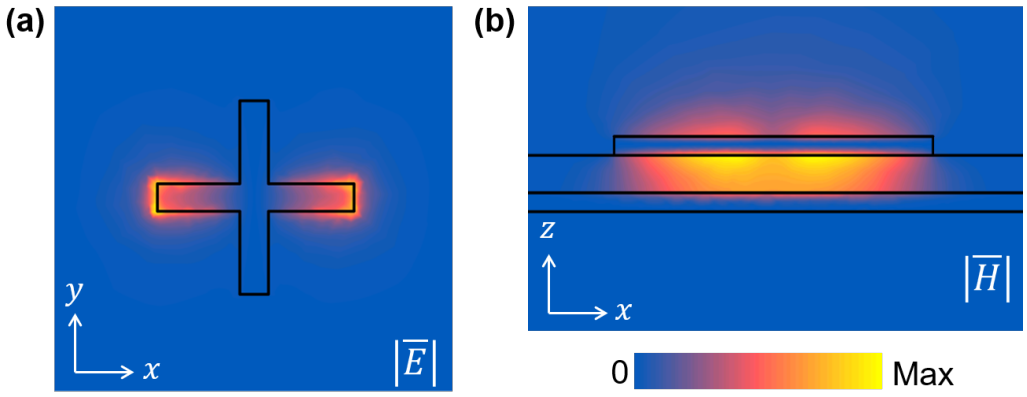

Figure 2.2: Simulated color maps of MIM IR absorbers with cross-shaped nanostructures. The electric and magnetic fields of the incident waves are polarized along the x-axis and y-axis, respectively. (a) The electric field intensity ($|E|$) from the top view and (b) the magnetic field intensity ($|H|$) from the cross-sectional view of a unit cell at the peak absorption.

The key properties of metamaterial IR absorbers include (1) absorptance, (2) bandwidth, (3) acceptance angle, and (4) polarization dependence. The absorptance is an important figure of merit for all IR absorbers and is used as a measure of how efficiently they absorb the delivered IR power. The MIM IR absorbers, in particular, are commonly referred to as 'perfect IR absorber' due to its near-unity absorption characteristic ($\eta \approx 100\%$) as many have reported. The absorption bandwidth of IR is a measure of spectral selectivity around peak absorption wavelength. It is commonly expressed in terms of the spectral distance between the two points where half of maximum absorption are located (full-width at half-maximum). Typically, non-resonant bulk absorbers exhibit

a wide bandwidth and are preferred when maximizing absorbed electromagnetic energy regardless of the spectral signatures is of the most importance (such as photovoltaics for energy harvesting applications). MIM IR absorbers, however, rely on the resonance of the electromagnetic waves in the plasmonic nanostructures and the subwavelength dielectric gap, and exhibit much narrower spectral bandwidths. Such absorbers with narrow spectral bandwidths are crucial for the applications where high spectral resolution is required to discriminate EM waves in a specific spectral signature of interests, such as mult-spectral imaging or spectroscopic sensing applications. The acceptance angle of the metamaterial absorbers determines the range of incident angles at which the absorber maintains a relatively high absorption without much degradation in absorptance or shift in peak absorption wavelength. Certain spectroscopic sensing devices based on surface plasmon resonance rely on excitation of angle-dependent surface plasmons on a grating surface; and they take advantage of such dependency on acceptance angle as it also directly relates to the spectral selectivity of the system. When it comes to other applications such as stand-off chemical detection, energy harvesting, or absorption spectroscopy, it is crucial to absorb as much of the impinging radiation as possible from a large solid angle. Furthermore, the sensitivity and efficiency of such systems are affected not only by the acceptance angle of the absorbers but also from the polarization of incident waves. Although certain applications such as optical communications may take advantage of polarization dependent absorption, absorption of incident IR of any arbitraty polarization is preferred to maximize the overall absorption efficiency. MIM IR absorbers can be designed to be insensitive to both angle and polarization of the incident waves, making them suitable for the implementation of a new class of compact, power-efficient, and spectrally selective IR detectors.

2.2 Analytical models

A thorough understanding of physical phenomenon in the MIM IR absorbers is crucial when designing application specific high performance absorbers. In this context, an accurate analytical modeling of the MIM IR absorbers is useful since it translates a complex absorption mechanism into a simpler form for easier analysis and study. In addition, such analytical models can serve as an accurate optimization design tool without the need of time consuming numerical computation. Unfortunately, many analytical models proposed to date fail to provide all the characteristic absorption properties such as absorption wavelength, absorptance, and absorption bandwidth simultaneously with deep understanding of comprehensive geometric parameters. Previously proposed models such as the interference theory, standing wave resonance model, for instance, explain the absorption

via multiple reflections in the dielectric spacer and calculate the absorption induced by dielectric loss; however, the model does not give insights to the geometric configurations of the plasmonic nanostructures or the electric dipole resonance between them [62, 66, 67]. On the other hand, the electrical circuit analogy attempts to interpret the plasmonic absorption as RLC resonance inside the system and the associated loss (Ohmic and dielectric losses). This is a powerful technique in that accurate modeling of the effective surface impedance via equivalent resonance circuit can be used in the transmission line theory to compute the absorption spectral response, allowing for the analysis of all absorption characteristics simultaneously. In this section, a new lumped equivalent circuit model is presented that is capable of accurately predicting the effective impedance and the spectral absorption response of the MIM IR absorbers via simple impedance matching theory. Sakurai et al. first proposed an RLC equivalent circuit model to describe the magnetic response of the MIM IR absorbers [63, 64]. It provides a helpful understanding of the MIM IR absorber, such as the location of peak absorption wavelengths. The single RLC resonance branch, consisting of lumped circuit elements as functions of width, length, and dielectric spacing, is capable of predicting the peak wavelength of an arbitrary MIM IR absorber. Nevertheless, the model lacks capability to generate spectral response of absorption in which one can analyze the peak wavelength, absorptance, and bandwidth of a given MIM IR absorber simultaneously. I attribute this shortcoming to the absence of the off-resonance reactance from capacitive coupling between neighboring unit cells. The modified circuit model proposed here models the additional reactance and provides accurate description of the effective impedance of the absorbers. It can be further utilized in the transmission line and its impedance matching theory to predict the condition for critical coupling and conjugate impedance matching that leads to a strong absorption. To validate the lumped equivalent model and design optimization, the results are directly compared with the experimental results in Chapter 3.

2.3 Equivalent Circuit Model

The modified lumped equivalent circuit (Figure 2.3) consists of the periodic capacitance (C_P) in series with an additional RLC circuit branch which models the magnetic dipole resonance. While C_P contributes to the electric dipole resonance and the out-of-resonance impedance level, the near-field coupling of localized plasmons and current loop are described in the magnetic dipole branch. C_P originates from the capacitive coupling between neighboring cross-shaped nanostructures, and is approximated by the capacitance between two neighboring wires (2.1) [68]. The magnetic dipole branch consists of a pair of mutual and kinetic inductance (L_m and L_k) and gap capacitances

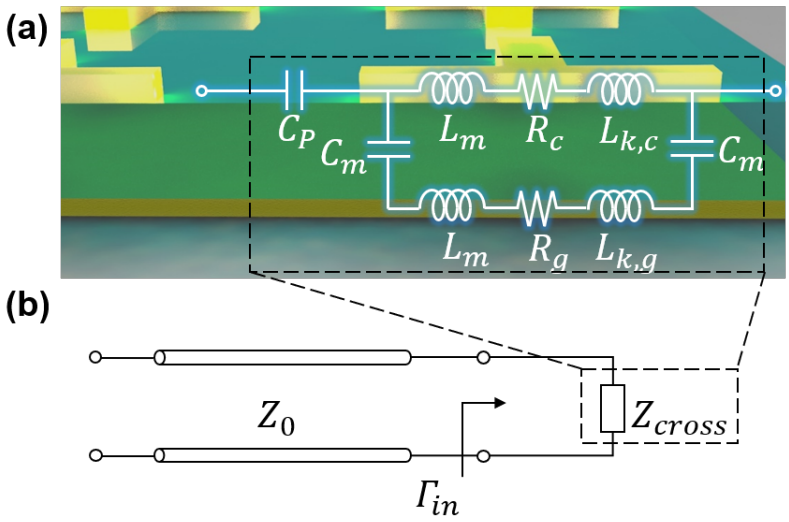

Figure 2.3: The lumped equivalent circuit model for MIM IR absorbers. (a) Cross-sectional view of the MIM IR absorber with lumped equivalent circuit model. (b) Transmission-line model of the MIM IR absorber.

(C_m) as well as the resistances of two metallic layers (R). In this thesis, gold is used for both top nanostructures and the ground plane. L_m and C_m take the forms of (2.2) and (2.3), respectively, where $\varepsilon_0 (\approx 8.854 \times 10^{-12} F/m)$ and $\mu_0 (= 4\pi \times 10^{-7} H/m)$ are permittivity and permeability of free space and ε_{ox} is the relative permittivity of silicon dioxide [69]. Note that $c (= 0.4 \sim 0.5)$ is a constant appropriately chosen to take the fringe effect of the capacitance and non-uniform electric field distribution into consideration (Figure 2.3.2) [63, 64]. The values of the effective lumped elements, determined using quasi-static considerations, are [7, 70–72]

$$C_P = \pi\varepsilon_0 \frac{a}{\ln\left(\frac{2(\Lambda-b)}{t_{Au}} + \sqrt{\left(\frac{2(\Lambda-b)}{t_{Au}}\right)^2 - 1}\right)} \tag{2.1}$$

$$L_m = \frac{1}{2}\mu_0 \frac{t_{ox} b}{a} \tag{2.2}$$

$$C_m = c\varepsilon_0\varepsilon_{ox} \frac{b}{2} \frac{a}{t_{ox}} \tag{2.3}$$

The above quasi-static expressions for the lumped elements assume waves impinging at normal incidence. Nevertheless, they can be expressed for an oblique incident angle by replacing the geometric dimensions ($\Lambda - b$ and t_{ox}) with effective parameters (Section 2.4). R and L_k in

the magnetic dipole branch arise from the real and imaginary part of impedance of the gold layers, respectively. Represented as an inductor in lumped circuit analogy, kinetic inductance of the gold layers models the phase delay in high frequency current flow, induced by the finite inertia of charge carriers in a conductive material (i.e., Au). This phenomenon is effectively described in the Drude conductivity model (2.4) as a function of DC conductivity (σ_{DC}), angular frequency (ω), and relaxation time (τ).

$$\sigma(\omega) = \frac{\sigma_{DC}}{1 + j\omega\tau} \tag{2.4}$$

In the Drude model, conductivity of a metal at high frequency regime is described as frequency dependent complex values, in which the real and imaginary parts contribute to the resistive and inductive components, respectively. That is, the impedance of the gold cross-type nanostructures is divided into two parts (real and imaginary parts) to form R_c and $L_{k,c}$ as lumped circuit elements as shown below (2.5).

$$Z_c = \frac{b'}{a\delta_{Au}} \frac{1}{\sigma_{Au}(\omega)} = \frac{b'}{a\delta_{Au}} \left(\frac{1 + j\omega\tau_{Au}}{\omega_p^2 \varepsilon_0 \tau_{Au}} \right) = R_c + j\omega L_{k,c} \tag{2.5}$$

The kinetic inductance of a conductive material can be derived in an alternative way, by equating its kinetic energy ($E_{kinetic} = \frac{1}{2} M_v^2$) and magnetic energy ($E_{magnetic} = \frac{1}{2} L_k I^2$). Here, M is the total mass of the charges and v is their velocity. The kinetic energy of gold cross-type nanostructures, therefore, can be expressed explicitly in terms of the geometric dimensions (a, b, δ_{Au}), electron mass (m_e), density (n), and charge (e) (2.6). Note that ω_p denotes the plasma frequency of gold and is written as $\omega_p = \sqrt{\frac{ne^2}{m_e \varepsilon_0}}$. Following the methods discussed above, one can express $L_{k,c}$ and R_c of the cross-type absorbers as shown in (2.8) and (2.9).

$$E_{kinetic} = \frac{1}{2} M v^2 = \frac{1}{2} \left(m_e n a \delta_{Au} b' \right) \left(\frac{I}{a\delta_{Au} bne} \right)^2 = \frac{1}{2} \left(\frac{b'}{a\delta_{Au}} \frac{1}{\omega_p^2 \varepsilon_0} \right) I^2 \tag{2.6}$$

$$E_{\text{magnetic}} = \frac{1}{2} L_{k,c} I^2 \tag{2.7}$$

$$L_{k,c} = \frac{b'}{a\delta_{Au}} \frac{1}{\omega_p^2 \varepsilon_0} \tag{2.8}$$

$$R_c = \frac{c'b}{a\delta_{Au}} \frac{1}{\sigma_{Au}} \tag{2.9}$$

Note that b' is the effective length of the cross nanostructures ($b' = c' \times b$), which is smaller than the designed length due to the uneven current distribution as shown in Figure 2.4. The

correction factor c' is approximated to be $c' = 1 - c$, which is related to the non-uniform electric field distribution. R_g and $L_{k,g}$ for the continuous ground plane can be derived in the same manner (2.10) and (2.11). However, the current distribution in the ground plane is different than that of the cross-shaped nanostructure, so we approximate the effective width (a') to be approximately half the length ($a' = 0.5 \times b$) of a cross-shaped nanostructure for calculations of R_g and $L_{k,g}$. The plasma frequency ($\omega_p \approx 2\pi \times 2.183 \times 10^{15} rad/s$) and relaxation time ($\tau_{Au} \approx 12.4 \times 10^{-15} s$) of gold are obtained from Rakic, A. D. et al. and are used to calculate the penetration depth (δ_{Au}) and DC conductivity (σ_{Au}) as described in (2.12) and (2.13), where λ and κ are the wavelength in free space and the extinction coefficient of gold, respectively [73–75].

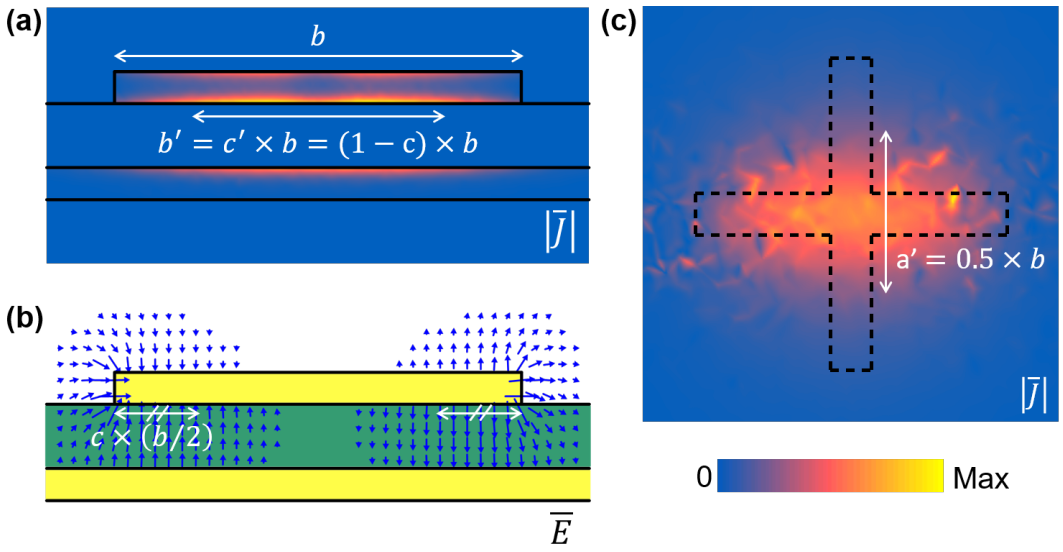

Figure 2.4: The effective geometric dimensions for the narrowband MIM IR absorbers. (a) The color map of the current density and (b) electric field distribution from cross-sectional view. (c) The color map of the current density in the continuous ground plane. The top nanostructure is outlined as dashed lines for reference. The double arrows indicate the effective dimensions used for lumped circuit elements.

$$L_{k,g} = \frac{b}{0.5 b \delta_{Au}} \frac{1}{\varepsilon_0 \omega_p^2} \tag{2.10}$$

$$R_g = \frac{b}{0.5 b \delta_{Au}} \frac{1}{\sigma_{Au}} \tag{2.11}$$

$$\delta_{Au} = \frac{\lambda}{2\pi\kappa} \tag{2.12}$$

$$\sigma_{Au} = \varepsilon_0 \omega_p^2 \tau_{Au} \tag{2.13}$$

It is worth noting that all lumped circuit elements are expressed in terms of geometric variables (a, b, t_{Au}andΛ) and material properties ($\varepsilon_{ox}, \omega_p, and \tau_{Au}$), which can guide the design and optimization of the absorbers. Finally, based on a conventional transmission-line model to describe the interaction with the impinging wave, we can calculate the absorptance (A) as $A = 1R_{\text{in}}$, where $R_{\text{in}}(= |\Gamma_{\text{in}}|^2 = |(Z_{\text{cross}} - Z_0)/(Z_{\text{cross}} + Z_0)|^2)$ is the reflectance and $Z_0(= \sqrt{\mu_0/\varepsilon_0} \approx 377\Omega)$ is the impedance of free space. When the value of Z_{cross} is close to the free space impedance ($Z_{\text{cross}} \approx Z_0$), R_{in} approaches zero, leading to near-unity absorption.

When designing the narrowband infrared absorbers for spectroscopy applications, the capability to tune the peak frequency is an important property. In this section, we take advantage of the modified circuit model to estimate the peak absorption frequency (f_{peak}) in terms of the circuit parameters. Note that the total impedance, $Z_{\text{cross}} = R_{\text{cross}}(\omega) + jX_{\text{cross}}(\omega)$, is a complex number ($R_{\text{cross}}(\omega)$and $X_{\text{cross}}(\omega)$ are the real and imaginary parts of $Z_{\text{cross}}(\omega)$, respectively) and therefore solutions do not necessarily exist when solving for $Z_{\text{cross}}(\omega) = Z_0 \approx 377 + j0\Omega$. Instead, we equate the imaginary part of the total impedance to zero, i.e. $X_{\text{cross}}(\omega) = 0$, to estimate the resonant frequency. The total impedance of the cross-type absorbers can be written as below in Laplace domain ($s = j\omega$), where Z_e and Z_m are the impedance of electric and magnetic dipole branches, respectively (2.14) - (2.16). Note that inductances for the gold nanostructures ($L_c = L_{k,c} + L_m$) and the continuous ground ($L_g = L_{k,g} + L_m$ plane are combined in the equations for simplicity. The real and imaginary parts of impedance of a cross-type absorber are plotted in Figure 2.5.

$$Z_{cross}(s) = Z_e + Z_m \tag{2.14}$$

$$\text{where } Z_e(s) = \frac{1}{sC_P} \tag{2.15}$$

$$Z_m(s) = \frac{s^3 C_m L_c L_g + s^2 C_m \left(L_c R_g + L_g R_c\right) + s\left(C_m R_c R_g + 2L_c\right) + 2R_c}{2 + s^2 C_m \left(L_c + L_g\right) + sC_m \left(R_c + R_g\right)} \tag{2.16}$$

To estimate the peak frequency, one can solve for $s_{\text{peak}} = j\omega_{\text{peak}} = j2\pi f_{\text{peak}}$ at which the imaginary part of $Z_{\text{cross}}(\omega)$ equal to zero. The estimated peak frequency can be expressed in terms of circuit parameters as below (2.17). The corresponding absorption spectrum is calculated using transmission line theory ($A = 1 - R_{\text{in}} = 1 - |\Gamma_{\text{in}}|^2 = 1 - |(Z_{\text{cross}} - Z_0)/(Z_{\text{cross}} + Z_0)|^2$) and shown in Figure 2.5 for comparison. Note that with the right level of loss to support critical coupling and conjugate matching, near unity absorption is achieved at the designed spectral band.

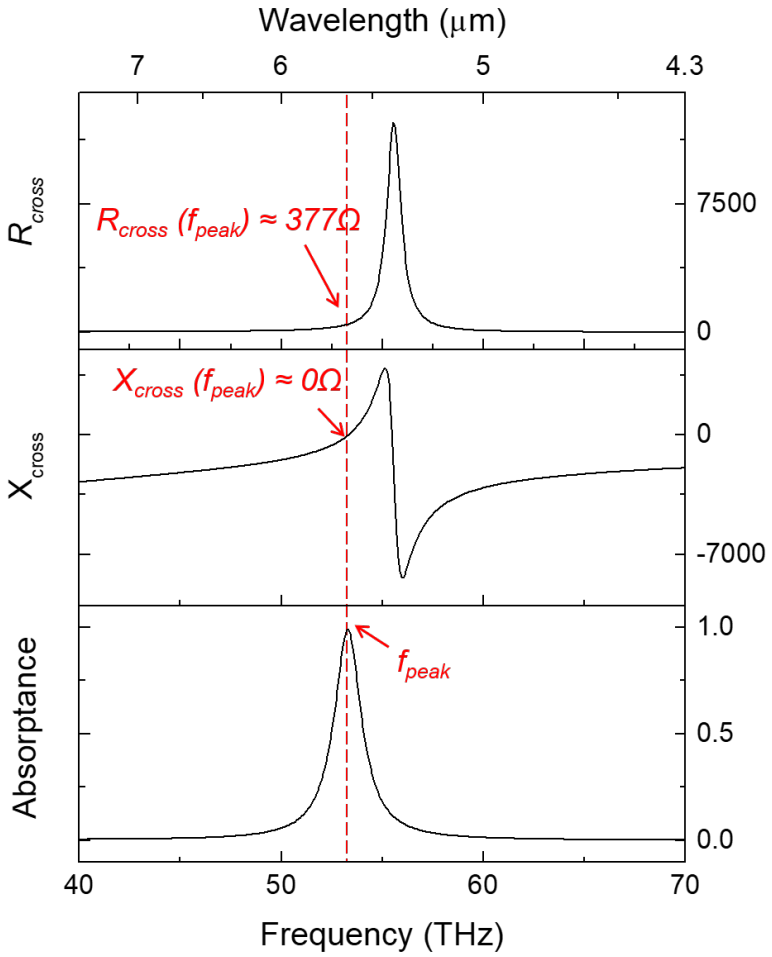

Figure 2.5: The real (R_{cross}) and imaginary (X_{cross}) parts of the circuit impedance (Z_{cross}) and the absorptance of a cross-type metamaterial infrared absorber. The peak absorption frequency of the absorber is approximately equal to the resonance of the RLC equivalent circuit, i.e. $X_{cross}|_{f=f_{\text{peak}}} \approx 0\Omega$ and $R_{\text{cross}} = |_{f=f_{\text{peak}}} \approx 377\Omega$

.

$$f_{\text{peak}} = \frac{1}{2\pi}\sqrt{\frac{1}{C_{\text{m}}\left(L_c + L_g\right)}} \cong \frac{1}{2\pi}\sqrt{\frac{1}{\text{C}_{\text{m}}\left(L_k + L_m\right)}} \tag{2.17}$$

Although it is not feasible to obtain exact closed-form solutions in terms of circuit parameters for the FWHM using transmission-line theory, one can estimate FWHM by evaluating the quality factor (Q) of the circuit ($Q \propto R_{\text{eq}}C_{\text{eq}}/L_{\text{eq}}$, where $R_{\text{eq}}, C_{\text{eq}}$, and L_{eq} are equivalent resistance, capacitance, and inductance of the circuit, respectively). As shown in (2.18) and (2.19), FWHM and fpeak (derived in (2.17)) can be further simplified and expressed in terms of geometric and material parameters of the cross-type absorbers.

$$\text{FWHM} \propto R\frac{C_P}{L_m + L_k} \propto \frac{a}{\tau_{Au}\ln(\Lambda)} \tag{2.18}$$

$$f_{\text{peak}} \propto \sqrt{\frac{1}{C_m\left(L_m + L_k\right)}} \propto \frac{1}{b} \tag{2.19}$$

(2.18) indicates that one can achieve narrow FWHM by maximizing Λ while reducing the width (a). However, the upper limit of Λ is set by the wavelength of operation (i.e.,$\Lambda < \Lambda_{\text{max}} = \lambda_{\text{peak}}/(1 + sin\theta)$, where $0 < \theta < 90°$is the angle of incidence), for Λ exceeding the limit will result in diffraction and the lumped equivalent circuit model is no longer valid [3, 76–79]. Note that this limit is more stringent (smaller Λ_{max}) at oblique incidence ($\theta > 0$), making the device more susceptible to diffraction. Therefore, to ensure strong absorption over a wide acceptance angle, we choose $\theta = 30°$ for the upper limit of Λ (e.g., $\Lambda_{\text{max}} \approx 4\ \mu m$ for $\lambda_{\text{peak}} = 6\mu m$). Figure 2.6 shows that an absorber with a wider Λ reaching its limit of $4\mu m$ results in a significant improvement, with up to 20% in selectivity. Furthermore, it implies that one can decrease FWHM by reducing a (i.e., larger b/a), up to the point when the absorption starts to decrease due to impedance mismatch ($Z_{\text{cross}} >> Z_0$ with smaller a), which sets the limit of scaling for a. In other words, when designing an optimized MIM IR absorber with a high spectral selectivity, both FWHM and absorption must be considered simultaneously. Since f_{peak} can be independently tuned by b, there exists a set of Λ and a at a given f_{peak} which guarantees a narrow FWHM and a near-unity absorption. Indeed, the MIM IR absorber with a larger periodicity ($\Lambda = 4.0\mu m$) and a narrower width ($a = 200nm$) demonstrates a significantly better spectral selectivity than the one with a smaller periodicity ($\Lambda = 2.5\mu m$) and a wider width ($a = 1700nm$) (Figure 2.6). I attribute this performance improvement based on geometric optimization to the minimization of cross-talk (due to the excessive capacitive coupling) between neighboring nanostructures (i.e. large Λ) and high length-to-width ratio (b/a) for strong plasmonic coupling and field confinement. In fact, wider absorption bandwidths (FWHM ¿ 20%)

have been commonly reported based on patch- or circular-type MIM IR absorbers, due to their relatively narrow Λ and b/a ratio [41, 47].

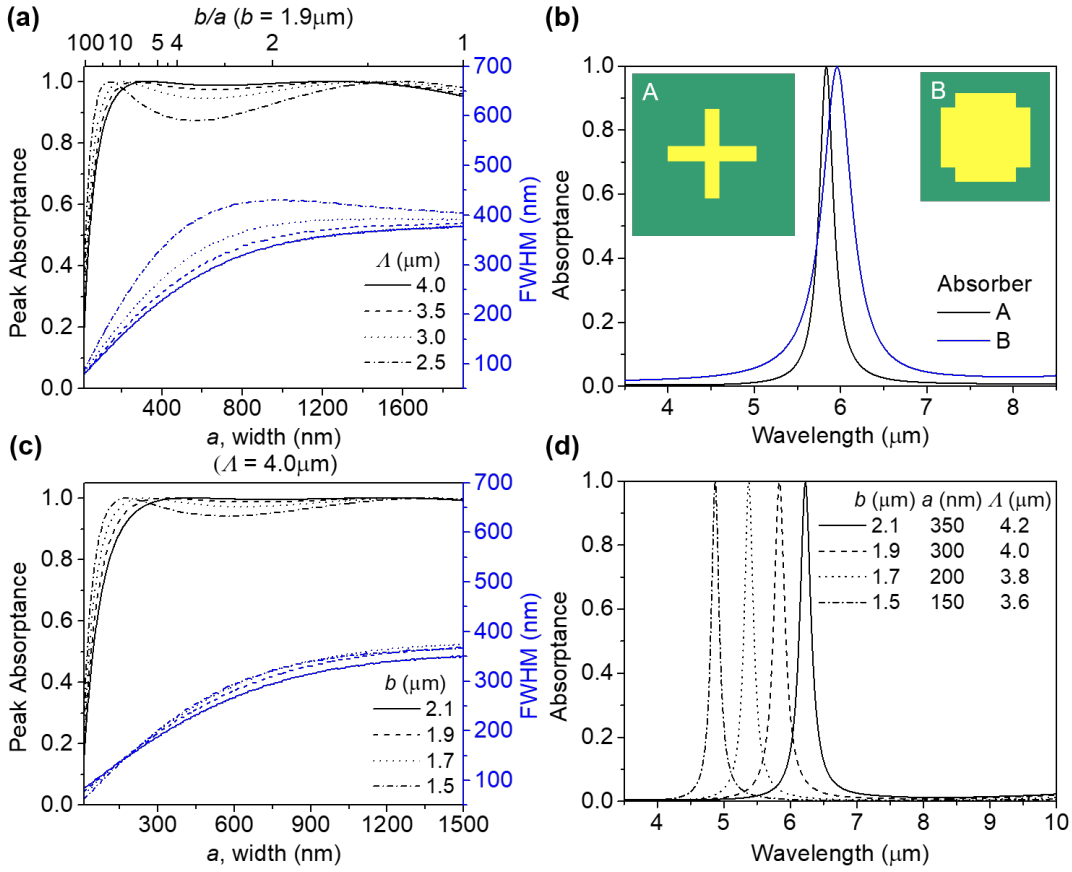

Figure 2.6: Optimization of MIM IR absorbers for high spectral resolution spectroscopy. (a) Calculated peak absorptance and FWHM with respect to the width and periodicity. (b) Comparison of the calculated absorption responses of the two MIM IR absorbers with different width and periodicity. The insets illustrate the geometric configurations of a unit cell for absorber A and absorber B. The lateral dimensions of the absorber A (B) are as follows: $b = 1900nm(1900nm)$, $a = 300nm(1700nm)$ and $\Lambda = 4.0\mu m(2.5\mu m)$. (c) Calculated peak absorptance and FWHM with respect to the width and length. (d) Calculated absorption responses of the lithographically-tuned MIM IR absorbers with optimized geometric dimensions.

2.4 Effective circuit parameters for oblique incident angles

Although the above absorption calculation based on transmission-line model assumes that the incident electromagnetic waves impinge at normal incidence ($\theta_{\mathrm{TM}} = \theta_{\mathrm{TE}} = 0°$), angular

absorption response can be approximated by using the effective geometric parameters. For an oblique incident angle, one may assume only the normal component of the incident waves contributes to the absorption response. Since the normal component of the wave vector ($k_\perp$) with an incident angle of θ_i, can be written as $k_\perp = kcos\theta_i$, we construct the effective geometric parameters for the gap between neighboring cross-shaped nanostructures ($\Lambda - b$) and the dielectric spacer (t_{ox}) for different polarizations. That is, for TM polarized waves, $\Lambda - b$ in C_P is replaced with $(\Lambda - b)/cos\theta_{\text{TM}}$; whereas for TE polarized waves, one can replace t_{ox} with $t_{\text{ox}}/cos\theta_{\text{TE}}$ in L_m and C_m as follows. Note that L_m and C_m for TM polarization (magnetic field is always parallel to the y-axis) and C_P for TE polarization (electric field is always parallel to x-axis) remain the same as those of normal incidence (2.20) - (2.22).

$$C_{P,TM} = \pi\varepsilon_0 \frac{a}{\ln\left(\frac{2\left(\frac{\Lambda-b}{\cos\theta_{TM}}\right)}{t_{Au}} + \sqrt{\left(\frac{2\left(\frac{\Lambda-b}{\cos\theta_{TM}}\right)}{t_{Au}}\right)^2 - 1}\right)} \tag{2.20}$$

$$L_{m,TE} = \frac{1}{2}\mu_0 \frac{\left(\frac{t_{ox}}{\cos\theta_{TE}}\right) b}{a} \tag{2.21}$$

$$C_{m,TE} = c\varepsilon_0\varepsilon_{ox}\frac{b}{2}\frac{a}{\left(\frac{t_{ox}}{\cos\theta_{TE}}\right)} \tag{2.22}$$

Chapter 3

Experimental Results

3.1 Fabrication

In this section, I show the fabrication process for 12 ultranarrow bandwidth MIM IR absorbers with lithographically-controlled peaks wavelengths on the same substrate. Each MIM IR absorber consists of an array of cross-type nanostructures in $150 \times 150\ \mu m^2$ fabricated on the same substrate (p-type silicon wafer), with the lateral dimensions (a, b, and Λ) as the only variables (Table 3.1). The geometric parameters of each absorber are optimized to exhibit narrowband (FWHM $\approx 3\%$) absorption. First, the ground plane is formed by electron beam (e-beam) evaporation of titanium-gold-titanium (10-100-10 nm). The first titanium (Ti) layer is to promote adhesion between the Si substrate and the gold (Au) ground plane, while the second Ti layer improves adhesion between the Au ground plane and the subsequent deposition of dielectric spacer. The subwavelength dielectric spacing is formed by deposition of silicon dioxide (SiO_2) using a PECVD (Plasma Enhanced Chemical Vapor Deposition) system. Next, lift-off-resist (LOR) and PMMA were spin-coated and e-beam lithography was performed to expose PMMA and pattern the desired cross-type nanostructures. It is worth noting that the two-material stack (LOR and PMMA) for patterning the nanostructure is adopted to prevent sidewall residues during the lift-off process, which may deteriorate the absorption selectivity (Section 3.2). After exposing, PMMA is developed using a MIBK:IPA (1:3) solution, followed by LOR development to form the desired undercuts. Finally, a 10-100 nm Ti-Au layer is deposited via electron beam evaporation and LOR-PMMA stack was removed by soaking the sample in photoresist remover at an elevated temperature. The cross-section schematic of the entire device fabrication process is shown in Figure 3.1.

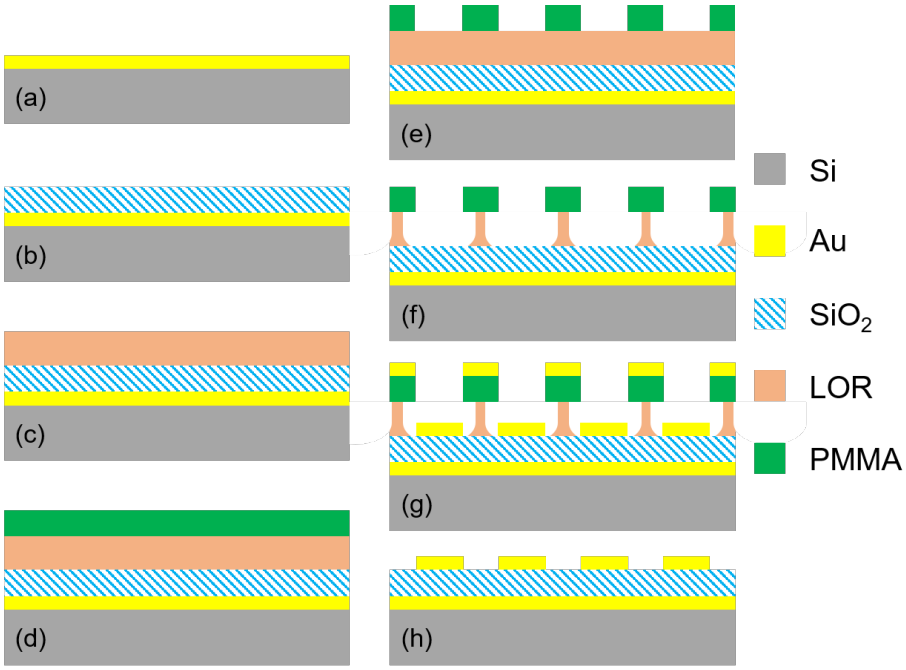

Figure 3.1: Cross-section schematics of the device fabrication process. (a) 100 nm gold is evaporated on a silicon substrate. (b) 200 nm silicon dioxide is deposited using plasma-enhanced chemical vapor deposition systems. (c) Lift-off-resist (LOR) is spin-coated and baked at $200°C$ for 5 minutes. (d) PMMA is spin-coated then exposed using an electron beam writing system. (e) PMMA is first developed using MIBK:IPA (1:3) solution for 60 seconds; (f) then LOR is etched to create the desired undercut using diluted TMAH-based developer. (g) 100 nm gold is evaporated. (h) Lift-off of LOR-PMMA stack to pattern the cross-type nanostructures.

Sample number	$\lambda_{\textbf{peak}}$ (μm)	**Width,** a (μm)	**Length,** b (μm)	**Periodicity** Λ (μm)
Absorber 1	4.27	150	1.3	3.0
Absorber 2	4.54	150	1.4	3.2
Absorber 3	4.89	200	1.5	3.4
Absorber 4	5.11	200	1.6	3.6
Absorber 5	5.36	200	1.7	3.6
Absorber 6	5.68	200	1.8	3.8
Absorber 7	5.83	200	1.9	4.0
Absorber 8	6.05	300	2.0	4.0
Absorber 9	6.27	300	2.1	4.0
Absorber 10	6.48	300	2.2	4.0
Absorber 11	6.63	300	2.3	4.0
Absorber 12	6.78	300	2.4	4.0

Table 3.1: Optimized lateral dimensions (a, b, and Λ) with respect to the measured peak absorption wavelength (λ_{peak}) of the 12 MIM IR absorbers for high spectral selectivity and absorptance

3.2 LOR-assisted E-Beam Lithography

The patterning of top plasmonic structures requires different techniques depending on the size of nanostructures (i.e., the peak absorption wavelengths of interests). In longer wavelength electromagnetic spectrum (typically in long wave infrared (LWIR), THz or higher), the size of nanostructures is in the order of a few or hundreds of μm (5 100 μm). For this reasons, conventional optical photolithography systems based on ultra violet (UV) rays can be used to pattern such structures. However, if the desired peak wavelengths are shorter than above (MWIR or shorter), the size of plasmonic structures becomes smaller than the minimum achievable feature size by optical photolithography due to the fundamental diffraction limit. Instead, electron beam lithography is a widely-used nano-fabrication technique to realize smaller feature sizes that can not be achieved by conventional optical lithography, capable of realizing nanometer-scaled resolution lithography (¡10 nm) with an extremely high accuracy. For this reason, e-beam lithography is suitable and widely adopted for patterning the sub-wavelength nanostructure shapes and dimensions in plasmonic and metamaterial applications. E-beam lithography process to pattern such nanostructures is typically accompanied by a lift-off or etching process of a thin film layer. Although the ease of characterization led to the popularity of lift-off process especially in academic research settings, the unwanted residues resulting from the lift-off process may degrade the performance for certain applications. The sidewall residue (also known as 'fencing') on the nanostructures of MIM IR absorbers, for instance, could result in increase of scattering of the impinging electromagnetic energy, hence lower absorption and widening of absorption bandwidth. Therefore, careful characterization of e-beam lithography and lift-off processes for the nanostructures of MIM IR absorbers is necessary for the application of high absorption and spectral resolution spectroscopy.

The absorbers in this thesis are fabricated with the bi-layer lift-off process, which drastically improves the reliability and repeatability of clean fabrication of the top nanostructures. The commercially available lift-off resist (LOR 3A) was spin-coated underneath the e-beam resist to assist the lift-off process for clean sidewall minimizing the scattering effect from the edges of gold nanostructures. It is worth noting that over-developing of lift off resist (LOR) layer may result in a collapse of LOR-poly(methyl methacrylate) (PMMA) stack, especially when the nanostructures are densely arranged. To avoid such problem, two step fabrication alterations were performed as detailed in Figure 3.1: (1) increasing baking temperature of LOR; and (2) developing with diluted tetramethylammonium hydroxide (TMAH)-based developer. First, LOR3A is spin-coated at 4000 rpm and baked on a $200^{\circ}C$ hot plate, followed by spin-coating of PMMA 950K at 5000 rpm and

baking on a $180°C$ hot plate. Next, PMMA is exposed with e-beam and developed in methyl isobutyl ketone (MIBK):isopropyl alcohol (IPA) (1:3) solution for 1 minute. The LOR layer is etched in a diluted AZ400K:DI water (1:1) developer for 4 miniutes. FInally, the Ti-Au is evaporated and patterned via lift-off in Remover PG heated at $80°C$. It is worth noting that the etch rate of LOR was slowed down to 1nm per second, which enabled a precise control of the undercut for such densely arranged nanostructures (Figure 3.2). The improved fabrication techniques indeed resulted in enhancement of absorptivity as well as spectral selectivity. As a comparison, patch-type MIM IR absorbers were fabricated using the single layer lift-off process (PMMA only) and the bi-layer lift-off process (LOR-PMMA stack). As shown in Figure 3.3, there is a significant improvement of LOR-assisted lift-off process, where the clean-fabrication of patch-type nanostructures allow for consistently high absorptance as well as high spectral selectivity compared to the patch-type nanostructures with uneven edges and residue from PMMA-only process.

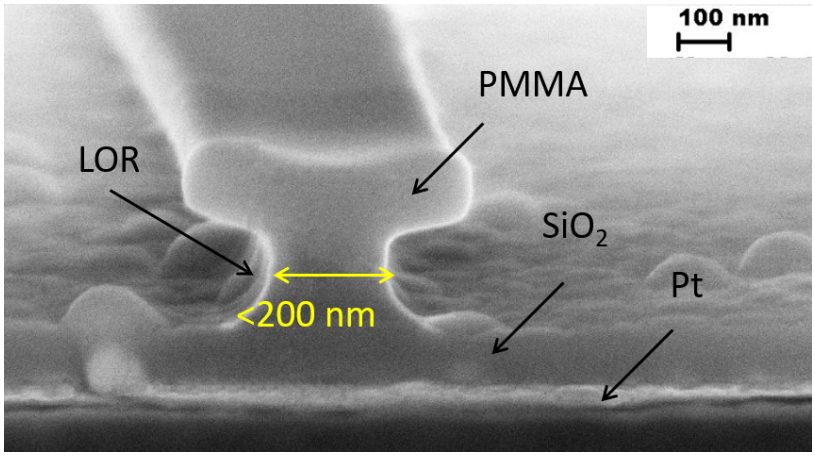

Figure 3.2: Cross sectional SEM image of PMMA-LOR stack. The sub-micron ($< 150nm$) width of LOR layer was realized with controlled etch of undercut.

3.3 Characterization

The reflectance spectra of the fabricated devices were measured using a Fourier transform infrared (FTIR) microscope (Bruker LUMOS FTIR Microscope). A reference measurement of the reflectance was first performed on the standard gold mirror. The raw reflectance measurements were then performed on the fabricated devices and normalized to the reference measurement in order to exclude atmosphere absorption. The size of knife-edge aperture was fixed at $\sim 100 \times 100\mu m^2$ for

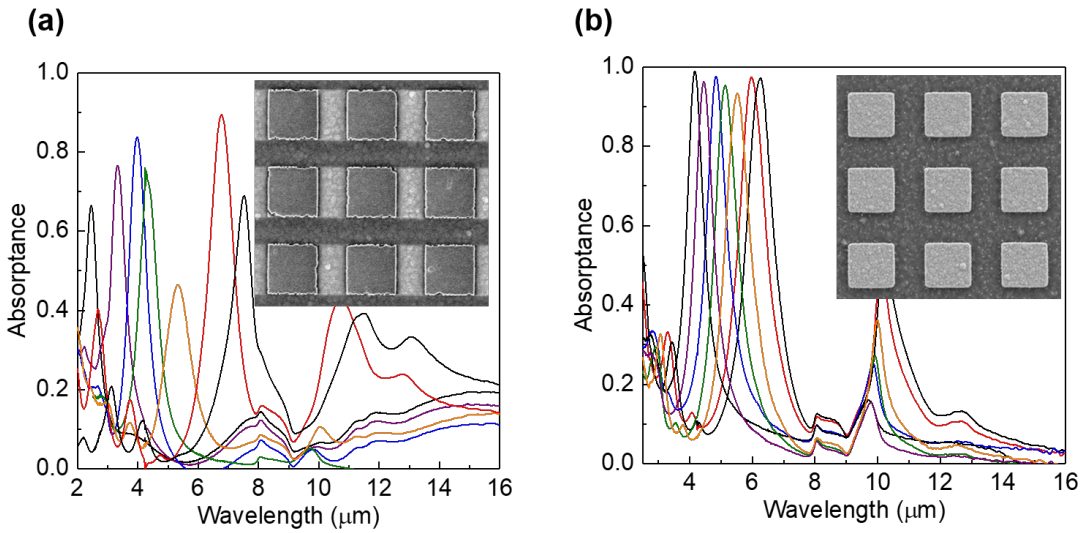

Figure 3.3: Measured absorption spectra of the patch-type MIM IR absorbers fabricated with (a) the single layer lift-off technique and (b) the bi-layer LOR-assisted lift-off technique.

both reference and device measurements. Absorption (A) was calculated by $A = 1 - R - T \approx 1 - R$, where R is the measured reflectance and T is the transmittance. The transmitted power is assumed to be negligible ($T \approx 0$), as the ground layer ($100nmAu$) of the fabricated absorbers is thicker than the penetration depth ($\delta_{Au} \approx 20nm$) at the working IR wavelengths.

3.4 Full wave numerical simulation

In this thesis, the finite integration technique, using the commercial software, Computer Simulation Technology (CST) Microwave Studio, was utilized to validate angular insensitivity as well as to study field distributions of the narrowband MIM IR absorbers. A unit cell with the periodic boundary settings was first constructed to simulate an array of the cross-shaped nanostructures. The Drude model material parameters for gold are obtained from Rakić, A. D. et al. and used for the cross-shaped nanostructures and the continuous ground plane [74]. The fitting parameters for Brendel oscillator to model optical properties of silicon dioxide were obtained from Kischkat, T. et al. [69]. The propagation direction of the waves is -z and both transverse electric (TE) and transverse magnetic (TM) polarization were taken into consideration by setting electric field parallel to x-axis and to y-axis, respectively Figure 2.2. The absorptance of unpolarized waves ($\eta_{unpolarized}$) was then calculated as $\eta_{unpolarized} \approx (\eta_{TE} + \eta_{TM})/2$, where η_{TE} and η_{TM} are absorptance of TE and

TM polarized waves, respectively. To simulate the angular sensitivity of the absorbers, the angle of incidence in the numerical simulation was swept from 0° to 70° with both TE and TM polarization

3.5 Results

The fabricated MIM IR absorbers via LOR-assisted e-beam lithography feature the residue-free plasmonic nanostructures as shown in Figure 3.4. Thanks to such improvement in fabrication technique, the absorptance spectra of the 12 narrowband MIM IR absorbers consistently demonstrate high absorptance ($\eta > 90\%$), narrow bandwidth ($FWHM < 4\%$) with the peak absorption wavelengths tunable in a wide MWIR region ($\lambda_0 = 4 \sim 7\mu m$) (Figure 3.5). Specifically, Figure 3.5-b highlights that an absorption bandwidth of only $180nm$ ($FWHM = 3.1\%$ at $\lambda_0 = 5.83\mu m$), the narrowest reported to date, and near perfect absorption ($\eta > 99.7\%$) are simultaneously obtained, while strong reflectance ($\eta \approx 0\%$) is achieved in the out-of-band spectral region. It is also worth noting that the lumped equivalent circuit model and the transmission line theory accurately predict the spectral response of the absorber from which one can obtain the bandwidth, peak wavelength and absorptance levels. The excellent agreement of measured peak absorption wavelengths and FWHM between the experimental results of all fabricated devices and those obtained by the corresponding modified circuit model is shown in Figure 3.6.

To demonstrate the potential impact of the optimized ultra-narrowband MIM IR absorbers for the development of high resolution and miniaturized IR spectrometers and multispectral imagers, we examine the spectral selectivity of the proposed absorbers as well as their polarization and angle sensitivity, specifically for trace gas sensing in MWIR. To highlight the capability of the proposed optimized narrowband MIM IR absorber to address the most stringent spectral resolution requirements for spectroscopy applications, the absorptance spectra of four optimized narrowband MIM IR absorbers are compared with the normalized emission spectra of four heated gases taken from HITRAN and NIST Chemistry WebBook (Figure 3.7) [80, 81]. The demonstrated ultra high spectral resolution allows each absorber to fully capture the IR signature of interest while rejecting the other densely located IR emissions. The calculated absorption spectra are also overlapped with the measurement results of the fabricated devices to further highlight the accuracy of the circuit model.

The polarization independence was experimentally demonstrated by measuring absorption spectra upon transverse electric (TE), transver magnetic (TM) and unpolarized (in the absence of a polarizer) incident waves using polarizer in FTIR microscope (Figure 3.8). It is shown that there

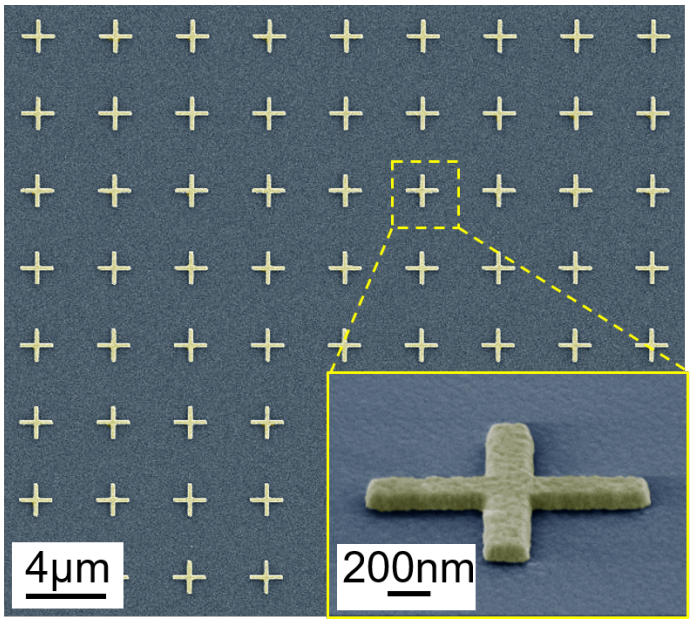

Figure 3.4: False colored SEM image of the ultra-narrowband MIM IR absorber. The inset is a close-up SEM image of a cross-shaped nanostructure, highlighting no-residue lift-off fabrication process.

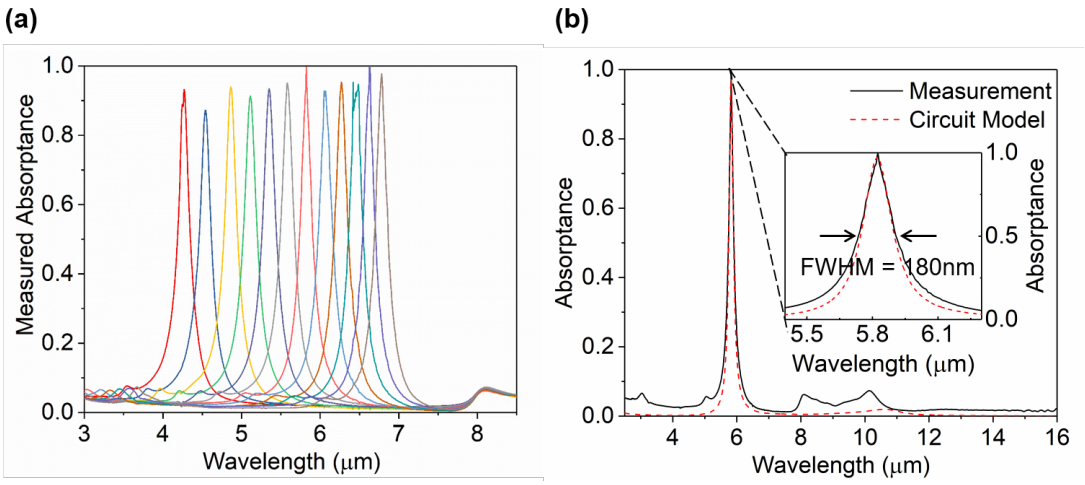

Figure 3.5: Experimental demonstration of narrowband MIM IR absorbers. (a) The measured absorption spectra of 12 narrowband MIM IR absorbers with lithographically tuned peak absorption. (b) The measured absorption spectrum (black solid line) of a fabricated absorber (Absorber 7, $\Lambda = 4.0\mu m$, $a = 200nm$, and $b = 1.9\mu m$) compared with the absorption spectrum predicted by the modified circuit model (red dashed line). The inset highlights the ultra-narrow FWHM reaching its theoretical limit of 3%.

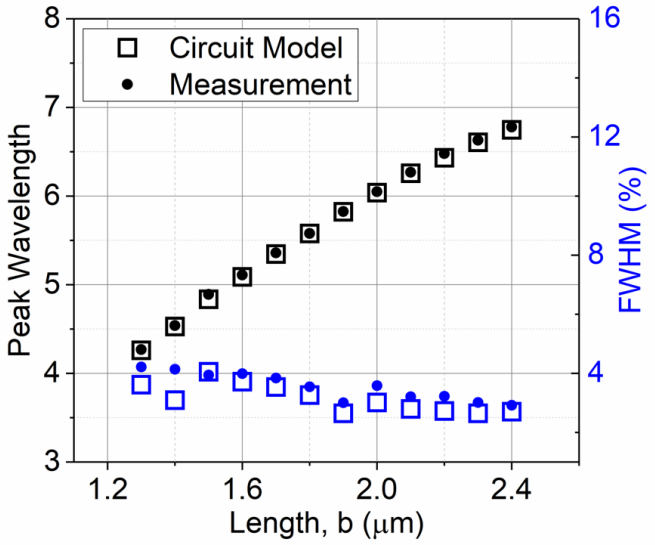

Figure 3.6: The experimental verification of peak wavelengths and FWHM of the 12 absorbers predicted by the circuit model.

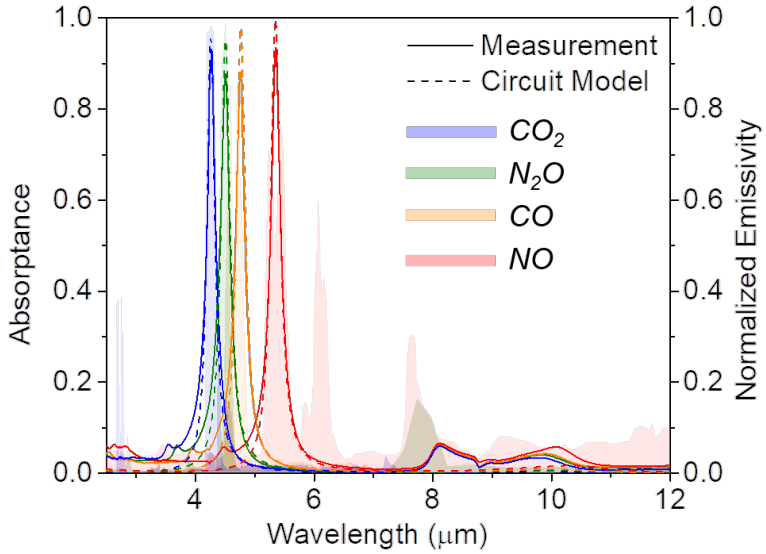

Figure 3.7: Graphical demonstration of non-disruptive MWIR gas spectroscopy based on the proposed narrowband MIM IR absorbers.

is little change in the absorption spectra between the three different polarizations of the incident IR, proving that the absorber is polarization independent. This is attributed to the 4-fold symmetric cross-shaped nanostructures. Due to the limited range of incident angles set by the objective lens of FTIR microscope ($\theta \approx 8 \sim 24^{\circ}$), the omnidirectional absorption is verified via equivalent circuit model and numerical calculation using CST. The full-wave simulation reveals that more than 70% absorption is maintained up to 60° of incident angle with little peak shift ($\Delta\lambda < 5\%$) (Figure 3.9). The demonstrated robust angular response of the absorber is therefore suitable for various standoff spectroscopic sensing applications that the angle of incidence is not in a limited solid angle. It is worth noting that the discrepancy observed in the angular dependency of the fundamental mode between the simulation and the circuit model is attributed to the onset of evanescent mode at higher incident angle, which is not predicted by the circuit model.

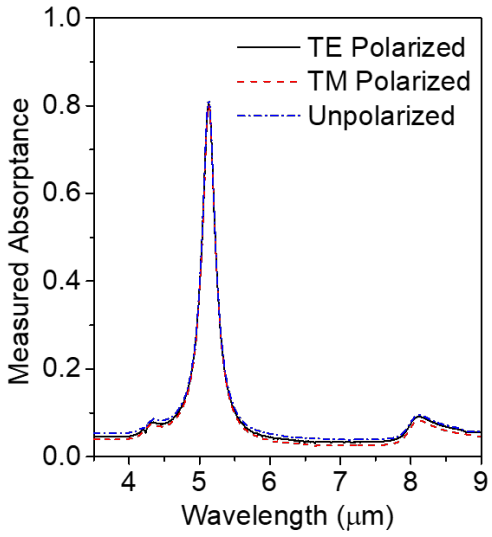

Figure 3.8: Demonstration of polarization insensitivity with the measured absorption spectra of a fabricated MIM IR absorber with and without polarizer of FTIR microscope.

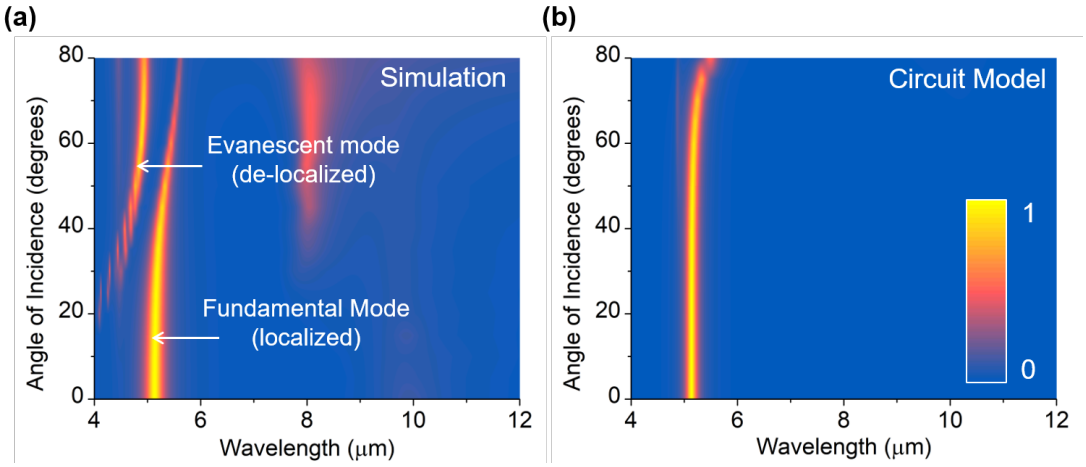

Figure 3.9: Absorption color maps with respect to the angle of incidence and wavelengths obtained by numerical simulation (a) and the modified circuit model. (b)

Chapter 4

Plasmonically-Enhanced Multispectral Infrared Microsystems

In the recent years of Internet of Things evolution, there has been increasing effort in sensor miniaturization due to the growing needs to build large sensor networks. With the advancement of micro and nanofabrication techniques, nano/micro electromechanical systems (N/MEMS) technologies have emerged as one of the best candidates to implement low-cost, miniaturized, and high performance sensors. IR sensing technologies are not an exceptionthe state of the art N/MEMS IR detectors are characterized by ultra-low noise IR detection and low power consumption in a form factor much smaller than the bulk electronic counterparts. In fact, they have been the key technologies for the high performance IR detector systems such as microbolometers, resonant IR detectors, and so on. One of the key components in such N/MEMS IR microsystems is a highly IR-absorbing material compatible with micro and nano fabrication. Although many bulk IR-absorbing materials are characterized by high absorption in IR regime, the absorption performance is inherently dependent on the intrinsic material properties. On the other hand, plasmonic IR absorbers such as MIM IR absorbers provide IR absorption characteristics that can not achieved by the bulk IR absorbing materials, as they feature lithographically defined spectral selectivity, near-unity absorption with polarization and angle insensitivity in a subwavelength thickness form factor. In this section,the two N/MEMS IR detector technologies that exploit the unique characteristics of plasmonic absorbers are presented: (1) spectrally selective aluminum nitride (AlN) resonant IR detectors; (2) zero-power micromechanical IR photoswitches.

4.1 MEMS-CMOS Multispectral Infrared Spectroscopic Sensors

In the past decade, IR spectroscopy has become a key technique in laboratory environments for accurate and non-disruptive analysis of chemical composition [82]. More recently, there has been a growing demand for exploring such IR spectroscopy technique beyond the traditional laboratory settings. In fact, the on-going trend in sensor development toward compact size, power efficiency, and reliable measurement has accompanied the increasing effort to implement ultra-miniaturized IR spectrometers, in lieu of the conventional IR spectrometers that are bulky, costly and power inefficient. The implementation of compact IR spectrometers can enable fast and accurate chemical composition analysis on-the-go, allowing for the IR spectroscopy technique to be easily accessible in diverse applications such as mobile food quality analysis and on-the-spot security screening. In this section, the first complete prototype of an ultra-miniaturized (total chip area $\approx 1.53mm^2$ multispectral IR chemical sensing microsystem comprising an array of plasmonically-enhanced MEMS IR detectors and a complementary metal oxide semiconductor (CMOS) IC readout is presented.

4.1.1 Spectrally Selective AlN Nano-Plate Resonant IR Detectors

One of the key elements for such miniaturized IR spectrometers is a high performance multispectral IR detector array with a chip-scale form factor and IR detection performance on par with the conventional uncooled IR detector technology. In this context, resonant IR detectors are the ideal candidates thanks to the fast response and high resolution enabled by their low noise performance, high thermal sensitivity and the use of frequency shift as the output parameter for high measurement accuracy [83]. N/MEMS resonant IR detectors exploit their unique electromechanical resonant properties, whose natural resonance frequency is sensitive to the external perturbation, to translate the absorbed IR energy into a measurable electrical read-out (resonance frequency shift). The high quality (Q) factor resonance and efficient electromechanical coupling allow for ultra-low noise performance, while significantly reducing the volume, cost, and complexity of the system. AlN resonant IR detector technology is particularly favored due to its unique advantages of volume scaling and compatibility with CMOS for on-chip frequency read-out [84, 85]. In fact, an AlN IR detector using silicon nitride as the dielectric IR absorbing material and a CMOS oscillator for direct frequency read-out has been reported [4]. Nevertheless, the use of such broadband IR absorbers prevents development of ultra-miniaturized IR spectrometers, as the system inevitably needs additional elements such as lasers or filters for spectral analysis.

The design of the IR absorber for such nano-plate resonators is particularly important since the top plate surface where IR irradiation impinges on is mostly covered by an optically thick IR-reflective material. The key design requirements for such IR absorbers include: (1) microfabrication compatibility; (2) ultra-thin thickness; (3) high absorptance; and (4) minimum degradation of electromechanical resonance performance. Furthermore, for stand-off IR spectroscopy applications, maximizing absorption efficiency is crucial, which is closely related to the polarization and angle dependence of the IR absorber. In this context, MIM IR absorbers are the ideal candidates in that they feature near-unity absorption and high spectral resolution while maintaining angle and polarization insensitivity. In fact, [86] has recently demonstrated the spectrally selective IR detectors based on the monolithic integration of MIM IR absorbers on top of AlN MEMS resonators.

4.1.2 Design and Fabrication

The sensor consists of five densely-packed MEMS resonant IR detectors wire-bonded to a CMOS read-out IC (Figure 4.1). The CMOS IC includes a self-sustained oscillator and an on-chip 3-bit decoder capable of addressing each detector through a switch bank [87]. The core element of the IR sensor is a thermally-sensitive AlN nano-plate resonator with an integrated nearly-perfect plasmonic absorber with lithographically-defined absorption wavelengths in MWIR regime. The resonant structures designed to vibrate at the same frequency are thermally-isolated from the substrate by nanoscale metallic anchors. The absorbed IR power causes a large and fast increase of the device temperature due to the high thermal resistance and extremely low thermal capacitance of the freestanding nanomechanical structure. The IR-induced temperature rise leads to a shift in the center frequency of the piezoelectric resonator due to its intrinsic temperature coefficient of frequency (TCF), which is monitored via the high stability oscillator CMOS IC.

The MIM IR absorbers, consisting of a 100-nm thick silicon dioxide layer sandwiched between the square-shaped nanostructure array and a ground plane, are integrated on the piezoelectric resonant nano-plates. Each of the five absorbers is individually optimized to achieve maximum IR absorptance in a specific MWIR band by lithographic tuning of lateral dimensions of the square-shaped plasmonic nanostructures. Computer Simulation Technology (CST) was used to verify the optimized absorption performance. The widths (w) and periodicities (Λ) of the five integrated plasmonic nanostructures are listed in Table 4.1.

The multiplexed CMOS readout circuity was taped-out in the ON Semiconductor $0.5-\mu m$ CMOS process. The proposed sensor was fabricated via a standard 4-mask microfabrication process

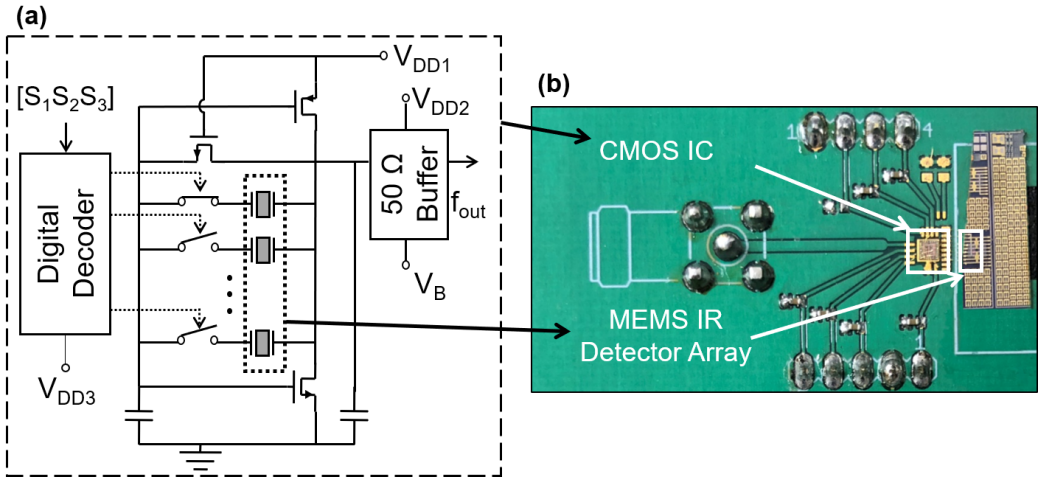

Figure 4.1: (a) Circuit diagram of the Pierce-like multiplexed oscillator with the integrated 3-bit on-chip decoder. (b) Image of the sensor consisting of the CMOS chip (area $\sim 1.05mm^2$) and the MEMS IR detector array (area $\sim 0.48mm^2$).

for the MEMS resonant IR detector array with an additional electron beam lithography step for the integrated plasmonic absorbers (Figure 4.2)). First, Pt interdigitated electrodes are patterend via e-beam evaporation and lift-off, followed by depositon of AlN (a). The Pt top electrode, which also serves as the ground plane for the MIM IR absorbers, is patterend via e-beam evaporation and lift-off (b). Next, AlN and SiO_2 are dry-etched (c); and gold probing pads are patterend via e-beam deposition and lift-off (d). The gold square-shaped plasmonic absorbers are patterned via e-beam lithography (e); and finally, the resonators are released by XeF_2 dry etch (f). The fabricated MEMS IR detector array has a ultra-compact footprint of $\sim 0.48mm^2$, thanks to the monolithic integration of the multispectral MIM IR absorbers (Figure 4.3).

Sample number	**Measured λ_{peak} (μm)**	**Width, w (μm)**	**Periodicity, Λ (μm)**
Absorber 1	3.3	0.8	1.5
Absorber 2	3.7	0.9	1.5
Absorber 3	4.4	1.1	2.2
Absorber 4	5.0	1.3	2.2
Absorber 5	5.7	1.5	2.2

Table 4.1: Lateral dimensions of the five integrated plasmonic absorbers.

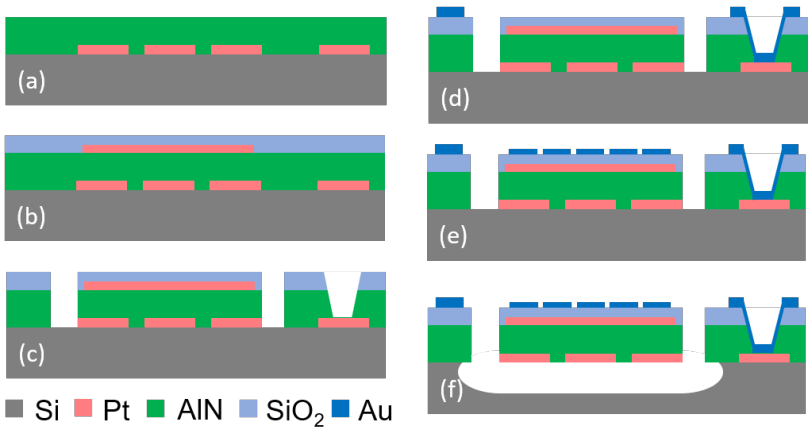

Figure 4.2: Microfabrication process of the MEMS detector array.

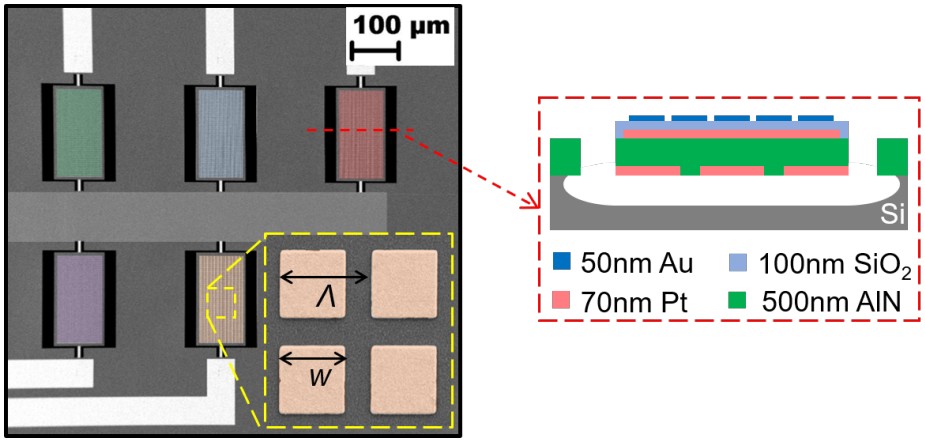

Figure 4.3: Scanning electron microscopic image of the IR detector array. The yellow inset shows a close-up view of the patch-type nanostructures of plasmonic absorber. The red inset shows a cross-section of an IR detector.

4.1.3 Experimental Results

The electromechanical performance of the fabricated MEMS resonant IR detectors was tested using an Agilent E5071 network analyzer. The admittance curve is fitted to modified Butterworth-Van Dyke (MBVD) model to extract equivalent electromechanical circuit pararmeters (Figure 4.4. The result shows a high mechanical quality factor (Q = 1778) and electromechanical coupling coefficient ($kt_2 = 1.78\%$) at the expected series resonance frequency at ($f_s = 240.86MHz$). Furthermore, the intrinsically high temperature coefficient of frequency of the resonator (TCF = 29.5 ppm/K) was measured on a temperature-controlled RF probe station by sweeping the temperature and monitoring the shift of resonance frequency (Figure 4.5).

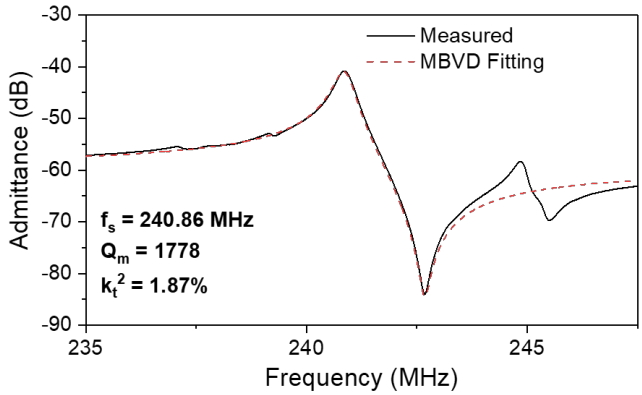

Figure 4.4: Measured admittance curve of an AlN IR detector and its modified Butterworth-Van Dyke model fitting.

The fabricated sensor was powered by a DC source ($V_{DD1} = 1.79V$) and its output signal was monitored over time with Agilent 53230A frequency counter. Each detector in the array was sequentially activated by the decoder to support self-sustained oscillation with a consistent output frequency $f_s \approx 241MHz$. A low noise performance of the oscillator circuit (Allan devication $\approx 7.4Hz$ at the optimal gate time of 100 ms) was measured as shown in Figure 4.5, leading to an ultra-low detection limit ($NEP \approx 402pW/Hz^{1/2}$) (Fig. 4c). The low power consumption of the prototpye ($\approx 1.07mW$) is measured by monitoring the current drawn from the power supply $\approx 600\mu A$.

The reflectance spectra (R) of the fabricated sensor was measured using a Bruker V70 Fourier transform infrared (FTIR) spectrometer coupled with a Hyperion 1000 IR microscope. The absorptance spectra (A) of the fabricated devices were then calculated assuming a negligible

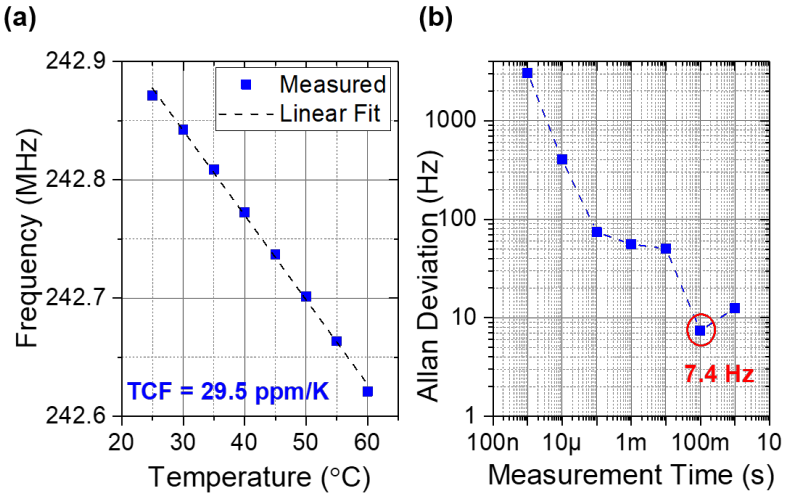

Figure 4.5: (b) Measured TCF ($\sim 29.5 ppm/K$) of the AlN IR detector. (d) Measured Allan deviation as a function of gate time, which corresponds to a noise-induced frequency fluctuation of $f_n \sim 2.34 Hz/Hz^{1/2}$ at the optimal gate time (100 ms).

transmitted power through the 70 nm optically-thick Pt reflector $A = 1R$. The large spectral range in MWIR ($\lambda_0 = 3 \sim 6\mu m$) was measured thanks to the monolithic integration of the MIM IR absorbers with lithographically-controlled peak absorption wavelengths (Figure 4.6). It is worth noting that the measured peak absorption wavelnegths show excellent agreement with the predicted peak absorption wavelengths obtained by the modified circuit model presented in Chapter 2. The results also show consistently high absorptance (η) up to 99.4% and a narrow FWHM down to 620 nm (Figure 4.6).

The sensor was then placed inside a vacuum chamber and its frequency output was monitored using the frequency counter. A calibrated blackbody at $600^{\circ}C$ (mechanically chopped at $\sim 1Hz$) was used as the broadband IR radiation source. The sensor was illuminated with the IR radiation transmitted through a $0.108 - mm$ thick zinc selenide liquid cell, containing either 100% acetone or hexane, and the calcium fluoride IR window of the vacuum cahmber (Figure 4.7).

The measured frequency shift of each IR detector in the array was normalized to that induced by the IR radiation without liquid cell to remove the effect from the variation of IR power of blackbody across the tested spectral bands (Figure 4.8). The IR-induced frequency shifts obtained by the proposed sensor successfully capture the spectral characteristics of the chemicals measured by the benchtop FTIR spectrometer. The demonstrated spectroscopic analysis in a significantly miniaturized form factor based on the proposed technology clearly emphasize the potential capability of the implementation of ultra-compact IR spectrometers.

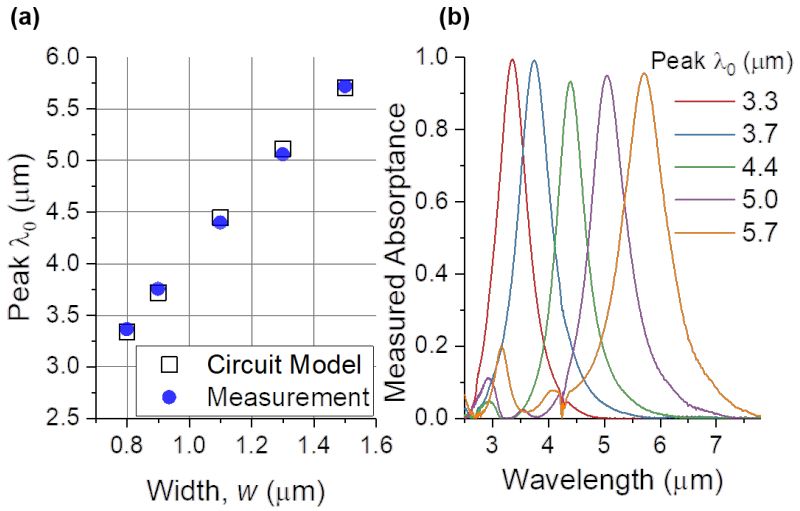

Figure 4.6: (a) Experimental verification of the lithographically tunable peak absorption wavelengths predicted by the equivalent circuit model. (b) Measured IR absorptance. Consistently high absorptance > 0.93 and narrow $FWHM < 890nm$ were measured across the five fabricated IR detectors.

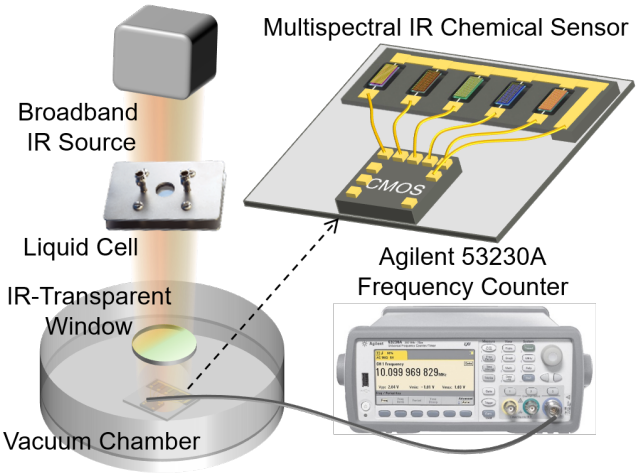

Figure 4.7: Schematic representation of the experimental setup. The sensor was placed inside a vacuum chamber and its frequency output was monitored using a frequency counter.

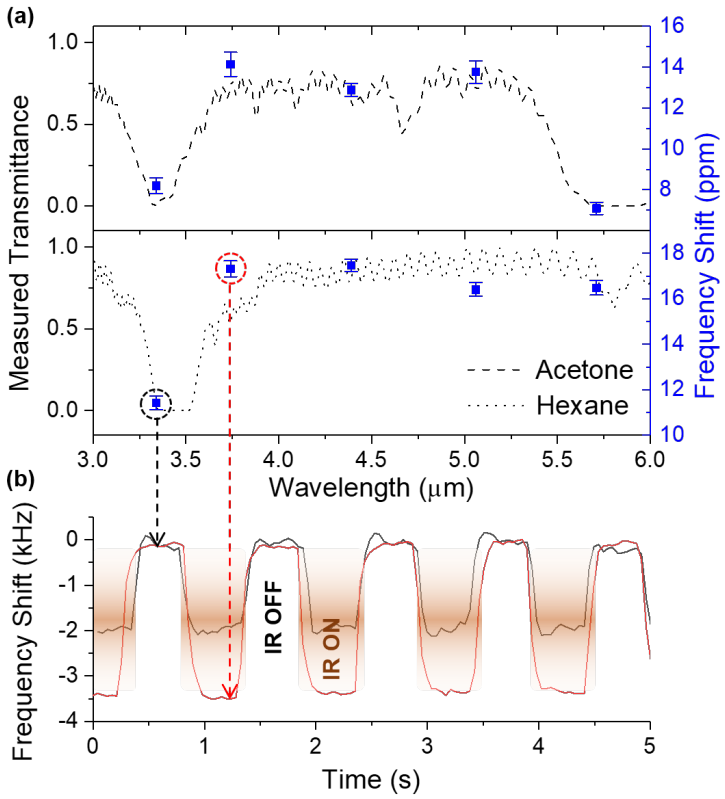

Figure 4.8: (a) Measured frequency shifts of the proposed sensor upon illumination of the IR radiation transmitted through the liquid cell containing acetone or hexane. The measurement uncertainty due to the output frequency instability is indicated by the error bars. (b) Measured frequency shifts of the IR detectors with the $3.3\mu m$ and $3.7\mu m$ IR absorption bands (black and red curves, respectively).

4.2 Zero-power Micromechanical Infrared Digitizer

Photoswitches detect presence of impinging light waves by converting the electromagnetic energy contained in the light to the electrical energy which can be used to detect, quatify, or anlayze the incident waves. They are used in a wide variety of applications including energy-saving and security purposes in both commercial and residential environments. The passive infrared (PIR) sensors, for instance, exploit pyroelectric materials such as gallium nitride (GaN), lithium tantalate ($LiTaO_3$)to detect temperature change and generate voltage upon IR irradiation. However, the intrinsic broadband absorption characteristic of such pyroelectric materials require external components such as narrowband filters to distinguish spectral contents in the impinging IR radiation. The spectral discrimination capability is especially crucial for the applications such as chemical IR detectors where the incident IR contains specific spectral signatures. Furthermore, such PIR sensors suffer from a limited sensor lifetime, which hinders the deployment of the sensors in a remote or inaccesible areas where consistent maintenance is generally to be avoided. This is attributed to the lack of integrated functionality that is capable of distinguishing a signature content from a target of interests in standby without a need of active circuitry, resulting in always-on state of the active detector regardless of the presence of the target of interests. In this context, the development of low-power and compact IR detectors that drastically reduce the 'idle power consumption is of a particular importance, especially in the emergent era of Internet of Things where a number of miniaturized sensors form a large and dense network. In this section, novel MEMS IR photoswitches that consume virtually no power at standby by only harvesting the IR energy contained in the spectral signature of interests. This built-in zero-power comparator function is realized via integrated spectrally selective metamaterial MIM IR absorbers, whose peak wavelengths, absorptance, and spectral bandwidth are lithographically controlled. The integrated MIM IR absorbers in the proposed zero-power multi-spectral IR digitizer are designed to detect and discriminate IR signature of exhaust gases coming out of a fuel-burning vehicle.

4.2.1 Design and Fabrication

The proposed IR digitizer is composed of 4 optically-actuated micromechanical switch (OMS)s connected in a logic circuit (Figure 4.9). Differently from existing switching elements, the OMSs rely on a plasmonically-enhanced thermomechanical coupling to selectively harvest the impinging optical energy in a specific spectral band of interests. The absorbed IR enregy is then used to mechanically create a conducting channel between the device terminals without any additional

power source, which directly translates into a zero-power consumption in standby ($< 1fW$). The prototypes presented here are selectively triggered by the narrow IR spectral bands centered at $\lambda = 3.4, 4.1, 4.5, and 5.6\mu m$ targeting the detection of IR signature of 4 kinds of exhaust gases (i.e., CO_2, CO, NO, and NO_2). The demonstrated large and abrupt change in conductivity (ON/OFF conduction ratio $> 10^{12}$) of the fabricated OMSs with an ultra-low switching threshold ($\sim 500nW$) and high reliability (> 6000 cycles recorded without failure) are suitable for the realization of a new class of zero-power IR digitizers capable of producing a quantized output bit in the presence of a unique IR spectral signature of interest.

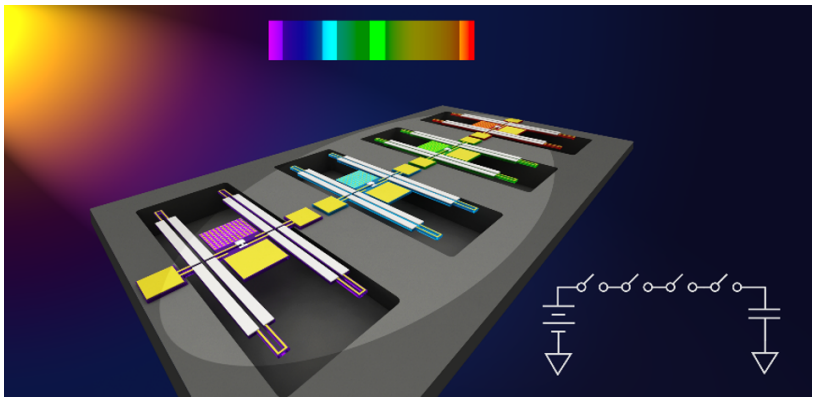

Figure 4.9: Visual illustration of 4 OMSs operating at different wavelengths connected in series to create a digital logic output.

The OMS consists of a pair of symmetric cantilevers, each composed of an IR-absorbing (or reflecting) head and an inner and outer pair of thermally sensitive bimaterial legs separated by a thermal isolation link as shown in Figure 4.10 [47]. The IR-absorbing head employs an MIM IR absorber with square-shaped plasmonic nanostructures for narrowband MWIR detection. The absorbed IR energy induces temperature rise in the inner pair of bimaterial legs and results in a downward displacement of the cantilever, bringing a high-stiffness Pt tip into contact with the opposite terminal. It is worth noting that the switch remains open until it absorbs IR energy in a specific spectral range (defined by the integrated MIM IR absorbers), regardless of the change in ambient temperature, thanks to the symmetric design of the two cantilevers. The sub-micron air gap maintained in standby translates directly into essentially zero leakage current and zero-standby power IR sensing. The 4 OMSs with different absorption wavelengths ($\lambda = 3.4, 4.1, 4.5, and 5.6\mu m$) were designed and fabricated using an 8-mask microfabrication process and e-beam lithography for plasmonic nanostructures [47]. Each integrated MIM IR absorber is optimized to absorb a specific IR

band by the lithographically defined lateral dimensions (w, Λ) of the plasmonic patch nanostructures.

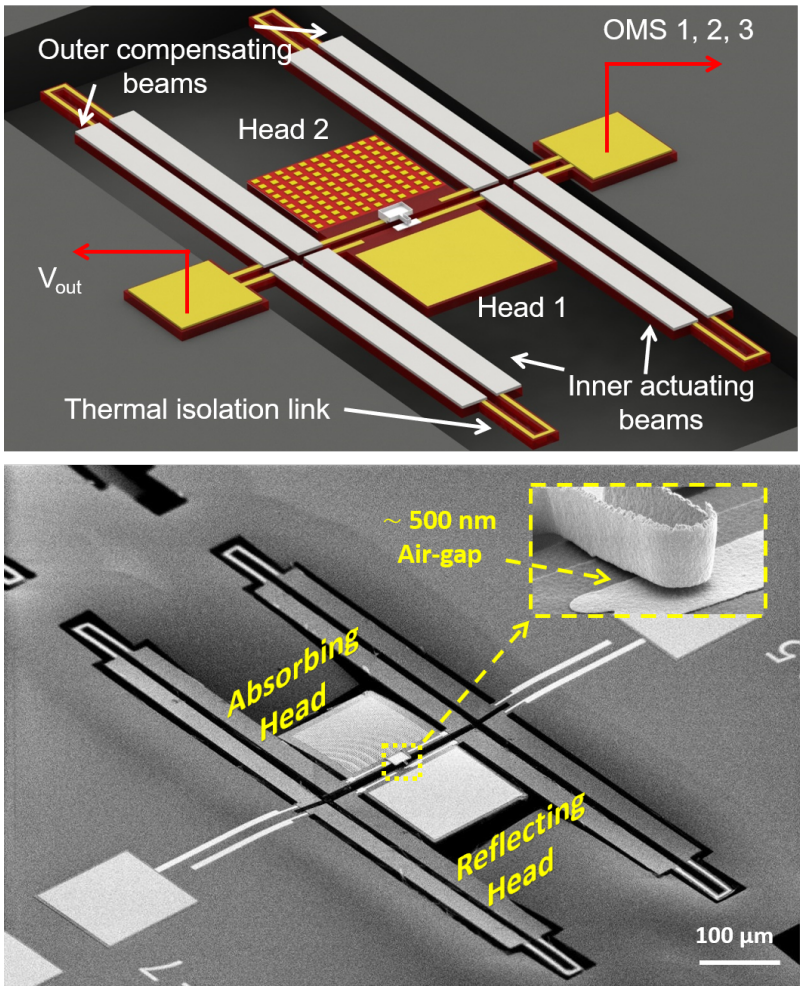

Figure 4.10: (a) Schematic representation of an optically-actuated micromechanical photoswitch; and (b) the SEM image of a fabricated optically-actuated micromechanical photoswitch. The inset highlights the high-stiffness Pt contact tip maintaining a sub-micron air gap from the bottom electrical contact.

4.2.2 Experimental Results

The absorption properties of fabricated devices were characterized showing high absorptance values $> 90\%$ with narrow bandwidths ($FWHM < 17\%$) (Figure 4.11). The IR response of the OMSs was tested using a calibrated blackbody IR source with filters centered at $3.5, 4.0, 4.5$, and $5.75\mu m$. The delivered power levels through each filter were estimated based on calibrated power density and absorber area at a given blackbody temperature. Figure 4.12 shows the measured current

response of the 4 OMSs upon blackbody IR radiation with the 4 filters and broadband radiation without a filter. The current was monitored while applying a constant bias voltage of $1mV$ for the $4.1, 4.5, 5.6\mu m$ OMSs, and $10mV$ for the $3.4\mu m$ OMS. The OMSs are designed to turn ON when the absorbed IR energy is above the designed threshold ($\sim 1\mu W$ for the $3.4, 4.1, 4.5\mu m$ OMSs and $\sim 500nW$ for the $5.6\mu m$ OMS). The delivered power for the $1\mu W$ threshold OMSs to turn ON is $1.1 \sim 1.5\mu W$; whereas the $500nW$ threshold device turned ON upon $\sim 600nW$ of delivered power.

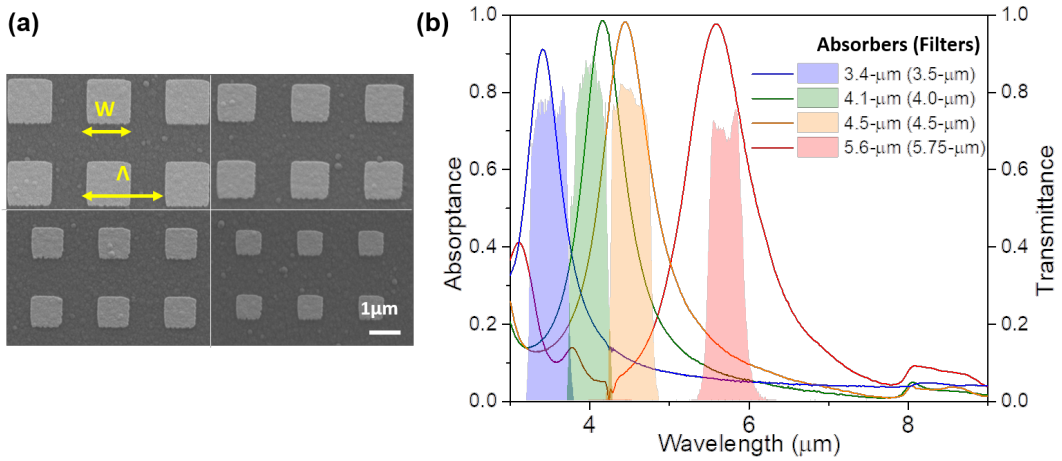

Figure 4.11: The 4 fabricated patch-type MIM IR absorbers integrated in the OMSs. (a) SEM image of the square-shaped nanostructures whose peak absorption wavelengths are individually controlled via lithography. (b) The FTIR measured absorption spectra of the 4 MIM IR absorbers, overlapped with the transmission spectra of the 4 optical filters centered at $3.5, 4.0, 4.5, and 5.75\mu m$. A consistently high absorption ($\eta > 90\%$) and narrow bandwidth ($FWHM < 17\%$) were recorded.

Each device only turned ON when illuminated by its in-band IR radiation with a power above the designed threshold, while it remained OFF when exposed to the same power but out-of-band IR radiations. The digitized outputs of the 4 devices corresponding to in-band and out-of-band radiations are summarized in Figure 4.13. The measured ON/OFF current (with a bias voltage of 1 and $10mV$) when exposed to chopped-IR radiation suggests a typical ON resistance of OMS $\sim 2.6k\Omega$. A large ON/OFF conductance ratio $> 10^{12}$ was also verified by the measurement of OFF-state leakage current ($< 5fA$) of a fabricated OMS. The achieved switching threshold of OMS is comparable to the one of the state-of-the-art IR wake-up switch, but the OMSs consume 9 orders of magnitude less power in stand by (near-zero power consumption) and is characterized by spectral selectivity and a significantly smaller form factor.

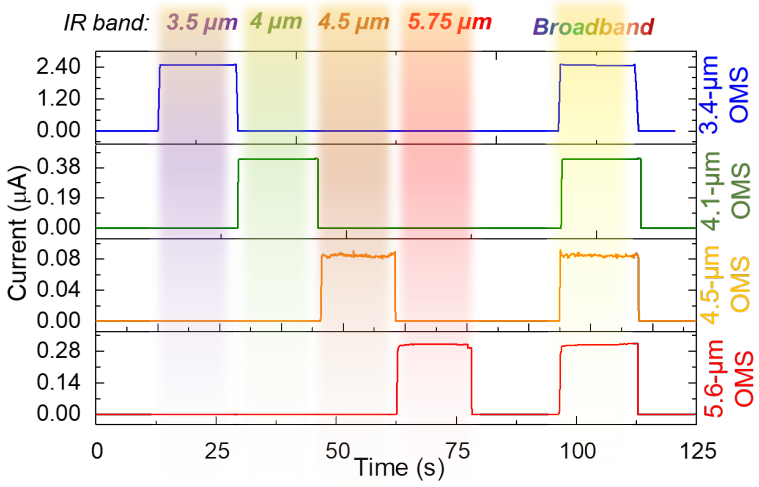

Figure 4.12: Measured ON/OFF current of the 4 OMSs in response to IR radiation through the 4 filters as well as to a broadband (unfiltered blackbody radiation) radiation.

Device	Infrared Spectral State				
	3.5μm Band	4.0μm Band	4.5μm Band	5.75μm Band	Broadband
3.4μm OMS	1	0	0	0	1
4.1μm OMS	0	1	0	0	1
4.5μm OMS	0	0	1	0	1
5.6μm OMS	0	0	0	1	1

Figure 4.13: The truth table of the 4-bit passive IR digitizer implemented by the four OMSs.

Chapter 5

Conclusion

In conclusion, this thesis presented the design and optimization of high performance narrowband MIM IR absorbers, suitable for the implementation of multispectral IR sensing microsystems (Chapter 2, Chapter 3). In Chapter 4, the two novel spectroscopic IR microsystems enabled by the narrowband MIM IR absorbers are introduced. The unique IR absorption characteristics of near-unity absorption, high spectral resolution, large angular acceptance, and polarization insensitivity realized in an ultra-thin form factor overcome the fundamental limitation of low IR absorption performance of the existing compact IR spectrometers based on photodiodes and Fabry-Perot interferometers. The high performance, miniaturized MIM IR absorbers can be seamlessly integrated in the existing detector technologies, resulting in a larger performance increase in IR detection capability. When designing such a high performance MIM IR absorber, a generalized analytical model that can predict the absorption response with specific process constraints such as lithography limits or material compatibility. In this context, the proposed lumped equivalent circuit model provides an accurate description of the effective surface impedance, allowing for the in-depth understanding of physical phenomena without the need of time-consuming numerical calculation tools. The modified circuit model takes the effect of dipole resonance between neighboring unit cells into consideration via the addition of periodic coupling capacitance C_P. The accurate description of the effective surface impedance is used in a transmission line model to analytically derive accurate spectral absorption response of the MIM IR absorbers. Based on the proposed circuit model, it is found that the cross-shaped nanostructures with a high length-to-width ratio and a wider periodicity lead to the narrow absorption bandwidth and near-unity absorption at peak wavelengths, reaching its predicted physical limit. The fabricated MIM IR absorbers consistently show narrow FWHM as small as 3.1%, with the peak absorption tunable in a wide IR spectral region, while maintaining high

absorptance, wide acceptance angle, and polarization insensitivity.

The monolithic integration capability of an array of multispectral absorbers is a key advantage in development of chip-scale IR spectroscopic microsystems. Indeed, many existing IR detector technologies exploit the lithographically controlled absorption in a sub-wavelength thickness form factor realized by the MIM IR absorbers, as they meet the stringent criteria for the implementation of miniaturized spectroscopic IR microsystems. For instance, the array of multispectral resonant IR detectors with the monolithically integrated MIM IR absorbers enable the spectrally selective IR detection while maintaining fast and low-noise IR detection performance thanks to the high quality resonance and the intrinsically high measurement accuracy based on monitoring of frequency shifts. The plasmonically-enhanced zero-power IR digitizers with the integrated MIM IR absorbers allow to maintain a sub-micron air gap when there is no useful IR signature present, which leads to a near-zero power consumption at standby. The monolithic integration of such OMSs with the integrated MIM IR absorbers presented allow for spectroscopic analysis without consuming any power at standby. In this context, the optimized MIM IR absorbers presented in the thesis would greatly improve the spectral selectivity of the pronounced metamaterial-enabled IR microsystems and allow for the implementation of miniaturized hyperspectral IR spectroscopic sensors.

Bibliography

[1] W. Dallenbach and W. Kleinsteuber, "Reflection and absorption of decimeter-waves by plane dielectric layers," *Hochfreq. u Elektroak*, vol. 51, pp. 152–156, 1938.

[2] W. W. Salisbury, "Absorbent body for electromagnetic waves," jun 1952.

[3] J. Pendry, A. Holden, W. Stewart, and I. Youngs, "Extremely low frequency plasmons in metallic microstructures," *Physical Review Letters*, vol. 76, no. 11, pp. 4773–4776, 1996. [Online]. Available: http://link.aps.org/doi/10.1103/PhysRevLett.76.4773

[4] D. R. Smith, "Metamaterials and Negative Refractive Index," *Science*, vol. 305, no. 5685, pp. 788–792, aug 2004. [Online]. Available: http://www.ncbi.nlm.nih.gov/pubmed/15297655{%}5Cnhttp://www.sciencemag.org/content/305/5685/788.shorthttp://www.sciencemag.org/cgi/doi/10.1126/science.1096796

[5] S. B. Glybovski, S. A. Tretyakov, P. A. Belov, Y. S. Kivshar, and C. R. Simovski, "Metasurfaces: From microwaves to visible," *Physics Reports*, vol. 634, pp. 1–72, 2016. [Online]. Available: http://www.sciencedirect.com/science/article/pii/S0370157316300618

[6] N. Engheta, "Thin absorbing screens using metamaterial surfaces," in *IEEE Antennas and Propagation Society International Symposium (IEEE Cat. No.02CH37313)*, vol. 2, no. June. IEEE, 2002, pp. 392–395. [Online]. Available: http://ieeexplore.ieee.org/document/1016106/

[7] A. Alù, A. Salandrino, and N. Engheta, "Parallel, series, and intermediate interconnections of optical nanocircuit elements 2 Nanocircuit and physical interpretation," *Journal of the Optical Society of America B*, vol. 24, no. 12, p. 3014, dec 2007. [Online]. Available: https://www.osapublishing.org/abstract.cfm?URI=josab-24-12-3014

[8] H. Luo, Y. Z. Cheng, and R. Z. Gong, "Numerical study of metamaterial absorber and extending absorbance bandwidth based on multi-square patches," *European Physical Journal B*, vol. 81, no. 4, pp. 387–392, 2011.

[9] C. Sabah, F. Dincer, M. Karaaslan, E. Unal, O. Akgol, and E. Demirel, "Perfect metamaterial absorber with polarization and incident angle independencies based on ring and cross-wire resonators for shielding and a sensor application," *Optics Communications*, vol. 322, pp. 137–142, 2014. [Online]. Available: http://dx.doi.org/10.1016/j.optcom.2014.02.036

[10] F. Hu, Y. Qian, Z. Li, J. Niu, K. Nie, X. Xiong, W. Zhang, and Z. Peng, "Design of a tunable terahertz narrowband metamaterial absorber based on an electrostatically actuated MEMS cantilever and split ring resonator array," *Journal of Optics*, vol. 15, no. 5, p. 55101, 2013. [Online]. Available: http://stacks.iop.org/2040-8986/15/i=5/a=055101?key=crossref.b7964fb880a0a36a402b3ef6f8946d50{%}5Cnpapers2://publication/doi/10.1088/2040-8978/15/5/055101

[11] H. Tao, N. I. Landy, C. M. Bingham, X. Zhang, R. D. Averitt, and W. J. Padilla, "A metamaterial absorber for the terahertz regime: design, fabrication and characterization," *Opt. Express*, vol. 16, no. 10, pp. 7181–7188, 2008. [Online]. Available: http://www.opticsexpress.org/abstract.cfm?URI=oe-16-10-7181

[12] H. Tao, C. M. Bingham, A. C. Strikwerda, D. Pilon, D. Shrekenhamer, N. I. Landy, K. Fan, X. Zhang, W. J. Padilla, and R. D. Averitt, "Highly flexible wide angle of incidence terahertz metamaterial absorber: Design, fabrication, and characterization," *Physical Review B - Condensed Matter and Materials Physics*, vol. 78, no. 24, pp. 2–5, 2008.

[13] J. Grant, Y. Ma, S. Saha, A. Khalid, and D. R. S. Cumming, "Polarization insensitive, broadband terahertz metamaterial absorber." *Optics letters*, vol. 36, no. 17, pp. 3476–3478, 2011.

[14] Y. Q. Ye, Y. Jin, and S. He, "Omnidirectional, polarization-insensitive and broadband thin absorber in the terahertz regime," *Journal of the Optical Society of America B*, vol. 27, no. 3, p. 498, feb 2010. [Online]. Available: http://www.osapublishing.org/viewmedia.cfm?uri=josab-27-3-498{&}seq=0{&}html=true

[15] I. Puscasu and W. L. Schaich, "Narrow-band, tunable infrared emission from arrays of microstrip patches," *Applied Physics Letters*, vol. 92, no. 23, pp. 98–101, 2008.

[16] H. Wang and L. Wang, "Perfect selective metamaterial solar absorbers," *Optics Express*, vol. 21, no. S6, pp. A1078–A1093, 2013. [Online]. Available: http://www.opticsexpress.org/abstract.cfm?URI=oe-21-106-A1078{%}5Cnhttps://www.osapublishing.org/oe/abstract.cfm?uri=oe-21-S6-A1078

[17] D. Wu, Y. Liu, and R. Li, "Infrared Perfect Ultra-narrow Band Absorber as Plasmonic Sensor," *Nanoscale Research Letters*, pp. 3–5, 2016. [Online]. Available: http://dx.doi.org/10.1186/s11671-016-1705-1

[18] G. Dayal and S. A. Ramakrishna, "Design of highly absorbing metamaterials for Infrared frequencies," *Optics Express*, vol. 20, no. 16, p. 17503, jul 2012. [Online]. Available: http://www.opticsexpress.org/abstract.cfm?URI=oe-20-16-17503https://www.osapublishing.org/oe/abstract.cfm?uri=oe-20-16-17503

[19] C. Hu, Z. Zhao, X. Chen, and X. Luo, "Realizing near-perfect absorption at visible frequencies." *Optics express*, vol. 17, no. 13, pp. 11 039–11 044, 2009.

[20] Y. Wang, T. Sun, T. Paudel, Y. Zhang, Z. Ren, and K. Kempa, "Metamaterial-plasmonic absorber structure for high efficiency amorphous silicon solar cells," *Nano Lett.*, vol. 12, no. 1, pp. 440–445, 2012.

[21] T. V. Teperik, F. J. García de Abajo, A. G. Borisov, M. Abdelsalam, P. N. Bartlett, Y. Sugawara, and J. J. Baumberg, "Omnidirectional absorption in nanostructured metal surfaces," *Nature Photonics*, vol. 2, no. 5, pp. 299–301, may 2008. [Online]. Available: http://dx.doi.org/10.1038/nphoton.2008.76http://www.nature.com/articles/nphoton.2008.76

[22] N. I. Landy, S. Sajuyigbe, J. J. Mock, D. R. Smith, and W. J. Padilla, "Perfect Metamaterial Absorber," *Physical Review Letters*, vol. 100, no. 20, p. 207402, may 2008. [Online]. Available: https://link.aps.org/doi/10.1103/PhysRevLett.100.207402

[23] J. Tak and J. Choi, "A Wearable Metamaterial Microwave Absorber," *IEEE Antennas and Wireless Propagation Letters*, vol. 16, pp. 784–787, 2017. [Online]. Available: http://ieeexplore.ieee.org/document/7556413/

[24] L. Zhao, H. Liu, Z. He, and S. Dong, "Theoretical design of twelve-band infrared metamaterial perfect absorber by combining the dipole, quadrupole, and octopole plasmon resonance modes

of four different ring-strip resonators," *Optics Express*, vol. 26, no. 10, p. 12838, 2018. [Online]. Available: https://www.osapublishing.org/abstract.cfm?URI=oe-26-10-12838

[25] J. Grant, M. Kenney, Y. D. Shah, I. Escorcia-Carranza, and D. R. S. Cumming, "CMOS compatible metamaterial absorbers for hyperspectral medium wave infrared imaging and sensing applications," *Optics Express*, vol. 26, no. 8, p. 10408, 2018. [Online]. Available: https://www.osapublishing.org/abstract.cfm?URI=oe-26-8-10408

[26] S. Kang, Z. Qian, V. Rajaram, A. Alu, and M. Rinaldi, "Ultra narrowband infrared absorbers for omni-directional and polarization insensitive multi-spectral sensing microsystems," in *2017 19th International Conference on Solid-State Sensors, Actuators and Microsystems (TRANSDUCERS)*. IEEE, jun 2017, pp. 886–889. [Online]. Available: http://ieeexplore.ieee.org/document/7994191/

[27] K. Üstün and G. Turhan-Sayan, "Ultra-broadband long-wavelength infrared metamaterial absorber based on a double-layer metasurface structure," *Journal of the Optical Society of America B*, vol. 34, no. 2, p. 456, 2017. [Online]. Available: https://www.osapublishing.org/abstract.cfm?URI=josab-34-2-456

[28] J. Nath, S. Modak, I. Rezadad, D. Panjwani, F. Rezaie, J. W. Cleary, and R. E. Peale, "Far-infrared absorber based on standing-wave resonances in metal-dielectric-metal cavity," *Optics Express*, vol. 23, no. 16, p. 20366, 2015. [Online]. Available: https://www.osapublishing.org/abstract.cfm?URI=oe-23-16-20366

[29] J. Nath, D. Maukonen, E. Smith, P. Figueiredo, G. Zummo, D. Panjwani, R. E. Peale, G. Boreman, J. W. Cleary, and K. Eyink, "Thin-film, wide-angle, design-tunable, selective absorber from near UV to far infrared," in *The International Society for Optical Engineering*, B. F. Andresen, G. F. Fulop, C. M. Hanson, P. R. Norton, and P. Robert, Eds., vol. 8704, no. June, jun 2013, p. 87041D. [Online]. Available: http://dx.doi.org/10.1117/12.2017958{%}5Cnhttp://proceedings.spiedigitallibrary.org/pdfaccess.ashx?ResourceID=5764345{&}PDFSource=24http://proceedings.spiedigitallibrary.org/proceeding.aspx?doi=10.1117/12.2017958

[30] H. Zhang, L. Feng, Y. Liang, and T. Xu, "An ultra-flexible plasmonic metamaterial film for efficient omnidirectional and broadband absorption," *Nanoscale*, 2018. [Online]. Available: http://pubs.rsc.org/en/Content/ArticleLanding/2018/NR/C8NR05276J

[31] H. A. Atwater and A. Polman, "Plasmonics for improved photovoltaic devices," *Nat. Mater.*, vol. 9, no. 10, pp. 865–865, 2010. [Online]. Available: http://dx.doi.org/10.1038/nmat2629{%}5Cnhttp://www.nature.com/doifinder/10.1038/nmat2866

[32] K. Aydin, V. E. Ferry, R. M. Briggs, and H. a. Atwater, "Broadband polarization-independent resonant light absorption using ultrathin plasmonic super absorbers," *Nature Communications*, vol. 2, p. 517, 2011. [Online]. Available: http://dx.doi.org/10.1038/ncomms1528

[33] Z. Li, S. Butun, and K. Aydin, "Ultranarrow band absorbers based on surface lattice resonances in nanostructured metal surfaces," *ACS Nano*, vol. 8, no. 8, pp. 8242–8248, 2014.

[34] Y. Qu, Q. Li, H. Gong, K. Du, S. Bai, D. Zhao, H. Ye, and M. Qiu, "Spatially and Spectrally Resolved Narrowband Optical Absorber Based on 2D Grating Nanostructures on Metallic Films," *Advanced Optical Materials*, vol. 4, no. 3, pp. 480–486, mar 2016. [Online]. Available: http://doi.wiley.com/10.1002/adom.201500651

[35] Y. L. Liao, Y. Zhao, X. Zhang, and Z. Chen, "An ultra-narrowband absorber with a compound dielectric grating and metal substrate," *Optics Communications*, vol. 385, no. November 2016, pp. 172–176, 2017. [Online]. Available: http://dx.doi.org/10.1016/j.optcom.2016.10.058

[36] Y. L. Liao and Y. Zhao, "Absorption Manipulation in a Narrowband Infrared Absorber Based on the Hybridization of Gap Plasmon and Fabry-Perot Resonance," *Plasmonics*, vol. 10, no. 5, pp. 1219–1223, 2015.

[37] D. Zhao, L. Meng, H. Gong, X. Chen, Y. Chen, M. Yan, Q. Li, and M. Qiu, "Ultra-narrow-band light dissipation by a stack of lamellar silver and alumina," *Applied Physics Letters*, vol. 104, no. 22, p. 221107, jun 2014. [Online]. Available: http://aip.scitation.org/doi/10.1063/1.4881267

[38] Y. Hui, Z. Qian, and M. Rinaldi, "Resonant infrared detector based on a piezoelectric fishnet metasurface," *2015 Joint Conference of the IEEE International Frequency Control Symposium and the European Frequency and Time Forum, FCS 2015 - Proceedings*, no. Figure 1, pp. 630–632, 2015.

[39] Y. Hui, J. S. Gomez-Diaz, Z. Qian, A. Alù, and M. Rinaldi, "Plasmonic piezoelectric nanomechanical resonator for spectrally selective infrared sensing," *Nature Communications*, vol. 7, p. 11249, apr 2016. [Online]. Available: http://www.nature.com/doifinder/10.1038/ncomms11249

[40] C. M. Watts, "Metamaterials and their applications towards novel imaging technologies," Ph.D. dissertation, 2015. [Online]. Available: http://login.ezproxy.library.ualberta.ca/login?url=http://search.proquest.com/docview/1719268970?accountid=14474{%}5Cnhttp://resolver.library.ualberta.ca/resolver?url{_}ver=Z39.88-2004{&}rft{_}val{_}fmt=info:ofi/fmt:kev:mtx:dissertation{&}genre=dissertations+{%}26+thes

[41] W. Yue, Z. Wang, Y. Yang, J. Han, J. Li, Z. Guo, H. Tan, and X.-X. Zhang, "High Performance Infrared Plasmonic Metamaterial Absorbers and Their Applications to Thin-film Sensing," *Plasmonics*, vol. 11, no. 6, pp. 1557–1563, dec 2016. [Online]. Available: http://dx.doi.org/10.1007/s11468-016-0210-9http://link.springer.com/10.1007/s11468-016-0210-9

[42] X. Liu, T. Tyler, T. Starr, A. F. Starr, N. M. Jokerst, and W. J. Padilla, "Taming the blackbody with infrared metamaterials as selective thermal emitters," *Physical Review Letters*, vol. 107, no. 4, pp. 4–7, 2011.

[43] C. M. Watts, X. Liu, and W. J. Padilla, "Metamaterial Electromagnetic Wave Absorbers," *Advanced Materials*, vol. 24, no. 23, pp. OP98–OP120, jun 2012. [Online]. Available: http://doi.wiley.com/10.1002/adma.201200674

[44] X. Liu, T. Starr, A. F. Starr, and W. J. Padilla, "Infrared spatial and frequency selective metamaterial with near-unity absorbance," *Physical Review Letters*, vol. 104, no. 20, pp. 1–4, 2010.

[45] X. Liu, "Infrared Metamaterial Absorbers: Fundamentals and Applications," PhD Thesis, Boston College, 2013. [Online]. Available: http://hdl.handle.net/2345/3829

[46] S. Ogawa and M. Kimata, "Metal-Insulator-Metal-Based Plasmonic Metamaterial Absorbers at Visible and Infrared Wavelengths: A Review," *Materials*, vol. 11, no. 3, p. 458, mar 2018. [Online]. Available: http://www.mdpi.com/1996-1944/11/3/458

[47] Z. Qian, S. Kang, V. Rajaram, C. Cassella, N. E. McGruer, and M. Rinaldi, "Zero-power infrared digitizers based on plasmonically enhanced micromechanical photoswitches," *Nature Nanotechnology*, vol. 12, no. 10, pp. 969–973, sep 2017. [Online]. Available: http://www.nature.com/doifinder/10.1038/nnano.2017.147

[48] V. Rajaram, Z. Qian, S. Kang, S. D. Calisgan, N. E. McGruer, and M. Rinaldi, "Zero-Power Electrically Tunable Micromechanical Photoswitches," *IEEE Sensors Journal*, vol. 18, no. 19, pp. 7833–7841, oct 2018. [Online]. Available: https://ieeexplore.ieee.org/document/8398460/

[49] A. Hubarevich, A. Kukhta, H. V. Demir, X. Sun, and H. Wang, "Ultra-thin broadband nanostructured insulator-metal-insulator-metal plasmonic light absorber," *Optics Express*, vol. 23, no. 8, p. 9753, apr 2015. [Online]. Available: https://www.osapublishing.org/abstract.cfm?URI=oe-23-8-9753

[50] J.-Y. Jung, K. Song, J.-H. Choi, J. Lee, D.-G. Choi, J.-H. Jeong, and D. P. Neikirk, "Infrared broadband metasurface absorber for reducing the thermal mass of a microbolometer," *Scientific Reports*, vol. 7, no. 1, p. 430, 2017. [Online]. Available: http://www.nature.com/articles/s41598-017-00586-x

[51] T. Maier and H. Brueckl, "Multispectral microbolometers for the midinfrared." *Optics letters*, vol. 35, no. 22, pp. 3766–3768, 2010.

[52] S. Zhang, W. Fan, K. J. Malloy, S. R. Brueck, N. C. Panoiu, and R. M. Osgood, "Near-infrared double negative metamaterials." *Optics express*, vol. 13, no. 13, pp. 4922–4930, 2005.

[53] S. Kang, Z. Qian, V. Rajaram, S. D. Calisgan, A. Alù, and M. Rinaldi, "Ultra-Narrowband Metamaterial Absorbers for High Spectral Resolution Infrared Spectroscopy," *Advanced Optical Materials*, vol. 1801236, p. 1801236, nov 2018. [Online]. Available: http://doi.wiley.com/10.1002/adom.201801236

[54] S. Luo, J. Zhao, D. Zuo, and X. Wang, "Perfect narrow band absorber for sensing applications," *Optics Express*, vol. 24, no. 9, p. 9288, 2016. [Online]. Available: https://www.osapublishing.org/abstract.cfm?URI=oe-23-16-20715{%}5Cnhttps://www.osapublishing.org/abstract.cfm?URI=oe-24-9-9288

[55] X. Lu, R. Wan, and T. Zhang, "Metal-dielectric-metal based narrow band absorber for sensing applications," *Optics Express*, vol. 23, no. 23, p. 29842, 2015. [Online]. Available: https://www.osapublishing.org/abstract.cfm?URI=oe-23-23-29842{%}5Cnhttps://www.osapublishing.org/oe/abstract.cfm?uri=oe-23-23-29842

[56] A. A. Jamali and B. Witzigmann, "Plasmonic Perfect Absorbers for Biosensing Applications," *Plasmonics*, no. May, pp. 1265–1270, 2014.

[57] H. H. Chen, Y. C. Su, W. L. Huang, C. Y. Kuo, W. C. Tian, M. J. Chen, and S. C. Lee, "A plasmonic infrared photodetector with narrow bandwidth absorption," *Applied Physics Letters*, vol. 105, no. 2, 2014.

[58] J. Y. Suen, K. Fan, J. Montoya, C. Bingham, V. Stenger, S. Sriram, and W. J. Padilla, "Multifunctional metamaterial pyroelectric infrared detectors," *Optica*, vol. 4, no. 2, p. 276, 2017. [Online]. Available: https://www.osapublishing.org/abstract.cfm?URI=optica-4-2-276

[59] E. Aslan, E. Aslan, M. Turkmen, and O. G. Saracoglu, "Metamaterial plasmonic absorber for reducing the spectral shift between near- and far-field responses in surface-enhanced spectroscopy applications," *Sensors and Actuators, A: Physical*, vol. 267, pp. 60–69, 2017. [Online]. Available: http://dx.doi.org/10.1016/j.sna.2017.10.006

[60] T. D. Dao, S. Ishii, T. Yokoyama, T. Sawada, R. P. Sugavaneshwar, K. Chen, Y. Wada, T. Nabatame, and T. Nagao, "Hole Array Perfect Absorbers for Spectrally Selective Midwavelength Infrared Pyroelectric Detectors," *ACS Photonics*, vol. 3, no. 7, pp. 1271–1278, jul 2016. [Online]. Available: http://pubs.acs.org/doi/abs/10.1021/acsphotonics.6b00249http://pubs.acs.org/doi/10.1021/acsphotonics.6b00249

[61] A. Lochbaum, Y. Fedoryshyn, A. Dorodnyy, U. Koch, C. Hafner, and J. Leuthold, "On-Chip Narrowband Thermal Emitter for Mid-IR Optical Gas Sensing," *ACS Photonics*, vol. 4, no. 6, pp. 1371–1380, jun 2017. [Online]. Available: http://pubs.acs.org/doi/10.1021/acsphotonics.6b01025

[62] X.-Y. Peng, B. Wang, S. Lai, D. H. Zhang, and J.-H. Teng, "Ultrathin multi-band planar metamaterial absorber based on standing wave resonances," *Opt. Express*, vol. 20, no. 25, pp. 27 756–27 765, 2012. [Online]. Available: http://www.opticsexpress.org/abstract.cfm?URI=oe-20-25-27756

[63] A. Sakurai, B. Zhao, and Z. M. Zhang, "Prediction of the Resonance Condition of Metamaterial Emitters and Absorbers Using Lc Circuit Model," in *Proceedings of 15th international heat transfer conference*, 2014, pp. 1–10.

[64] A. Sakurai, B. Zhao, and Z. M. Zhang, "Resonant frequency and bandwidth of metamaterial emitters and absorbers predicted by an RLC circuit model," *Journal of Quantitative Spectroscopy and Radiative Transfer*, vol. 149, pp. 33–40, dec 2014. [Online].

Available: http://dx.doi.org/10.1016/j.jqsrt.2014.07.024http://linkinghub.elsevier.com/retrieve/pii/S0022407314003306

[65] S. A. Tretyakov and C. R. Simovski, "Dynamic Model of Artificial Reactive Impedance Surfaces," *Journal of Electromagnetic Waves and Applications*, vol. 17, no. 1, pp. 131–145, 2003. [Online]. Available: http://www.tandfonline.com/doi/abs/10.1163/156939303766975407

[66] T. Wanghuang, W. Chen, Y. Huang, and G. Wen, "Analysis of metamaterial absorber in normal and oblique incidence by using interference theory," *AIP Advances*, vol. 3, no. 10, p. 102118, oct 2013. [Online]. Available: http://aip.scitation.org/doi/10.1063/1.4757879http://aip.scitation.org/doi/10.1063/1.4826522

[67] H.-T. Chen, "Interference theory of metamaterial perfect absorbers," *Optics Express*, vol. 20, no. 7, p. 7165, 2012.

[68] J. D. Jackson, *Classical electrodynamics*, 2nd ed. New York: New York : Wiley, 1975.

[69] J. Kischkat, S. Peters, B. Gruska, M. Semtsiv, M. Chashnikova, M. Klinkmüller, O. Fedosenko, S. Machulik, A. Aleksandrova, G. Monastyrskyi, Y. Flores, and W. Ted Masselink, "Mid-infrared optical properties of thin films of aluminum oxide, titanium dioxide, silicon dioxide, aluminum nitride, and silicon nitride," *Applied Optics*, vol. 51, no. 28, p. 6789, 2012.

[70] N. Engheta, A. Salandrino, and A. Alù, "Circuit Elements at Optical Frequencies: Nanoinductors, Nanocapacitors, and Nanoresistors," *Physical Review Letters*, vol. 95, no. 9, p. 095504, aug 2005. [Online]. Available: https://link.aps.org/doi/10.1103/PhysRevLett.95.095504http://www.ncbi.nlm.nih.gov/pubmed/16197226

[71] B. A. Munk, *Frequency Selective Surfaces*. Hoboken, NJ, USA: John Wiley & Sons, Inc., apr 2000. [Online]. Available: http://doi.wiley.com/10.1002/0471723770

[72] Y. P. Lee, J. Y. Rhee, Y. J. Yoo, and K. W. Kim, *Metamaterials for Perfect Absorption*, ser. Springer Series in Materials Science. Singapore: Springer Singapore, 2016, vol. 236. [Online]. Available: http://link.springer.com/10.1007/978-981-10-0105-5

[73] Y. Zhong, D. Wasserman, Y. Zhong, S. D. Malagari, T. Hamilton, and D. Wasserman, "Review of mid-infrared plasmonic materials Review of mid-infrared plasmonic materials," *Journal of Nanophotonics*, vol. 9, p. 093791, 2015.

[74] A. D. Rakić, A. B. Djurišić, J. M. Elazar, and M. L. Majewski, "Optical properties of metallic films for vertical-cavity optoelectronic devices," *Applied Optics Optics*, vol. 37, no. 22, pp. 5271–5283, 1998. [Online]. Available: http://ao.osa.org/abstract.cfm?URI=ao-37-22-5271

[75] S. A. Maier, *Plasmonics: Fundamentals and Applications*. New York, NY: Springer US, 2007. [Online]. Available: http://link.springer.com/10.1007/0-387-37825-1

[76] D. R. Smith, S. Schultz, P. Markoš, and C. M. Soukoulis, "Determination of effective permittivity and permeability of metamaterials from reflection and transmission coefficients," *Physical Review B*, vol. 65, no. 19, p. 195104, 2002. [Online]. Available: http://link.aps.org/doi/10.1103/PhysRevB.65.195104

[77] X. Zhang and Y. Wu, "Effective medium theory for anisotropic metamaterials," *Scientific Reports*, vol. 5, no. 1, p. 7892, jul 2015. [Online]. Available: http://www.nature.com/articles/srep07892

[78] J. B. Pendry, A. J. Holden, D. J. Robbins, and W. J. Stewart, "Magnetism from conductors and enhanced nonlinear phenomena [J]," *IEEE Transactions on Microwave Theory and Techniques*, vol. 47, no. 11, pp. 2075–2084, 1999.

[79] R. S. Longhurst, *Geometrical and physical optics*. New York, NY: Wiley, 1967.

[80] L. S. Rothman, I. E. Gordon, A. Barbe, D. C. Benner, P. F. Bernath, M. Birk, V. Boudon, L. R. Brown, A. Campargue, J. P. Champion, K. Chance, L. H. Coudert, V. Dana, V. M. Devi, S. Fally, J. M. Flaud, R. R. Gamache, A. Goldman, D. Jacquemart, I. Kleiner, N. Lacome, W. J. Lafferty, J. Y. Mandin, S. T. Massie, S. N. Mikhailenko, C. E. Miller, N. Moazzen-Ahmadi, O. V. Naumenko, A. V. Nikitin, J. Orphal, V. I. Perevalov, A. Perrin, A. Predoi-Cross, C. P. Rinsland, M. Rotger, M. Šimečková, M. A. Smith, K. Sung, S. A. Tashkun, J. Tennyson, R. A. Toth, A. C. Vandaele, and J. Vander Auwera, "The HITRAN 2008 molecular spectroscopic database," *Journal of Quantitative Spectroscopy and Radiative Transfer*, vol. 110, no. 9-10, pp. 533–572, 2009.

[81] P. Listrom and W. Mallard, "NIST Chemistry WebBook." [Online]. Available: http://webbook.nist.gov/chemistry/

[82] A. Fried and D. Richter, "Infrared Absorption Spectroscopy," in *Analytical Techniques for Atmospheric Measurement*. Oxford, UK: Blackwell Publishing, 2007, pp. 72–146. [Online]. Available: http://doi.wiley.com/10.1002/9780470988510.ch2

[83] V. J. Gokhale and M. Rais-Zadeh, "Uncooled Infrared Detectors Using Gallium Nitride on Silicon Micromechanical Resonators," *Journal of Microelectromechanical Systems*, vol. 23, no. 4, pp. 803–810, aug 2014. [Online]. Available: http://ieeexplore.ieee.org/document/6680650/

[84] Z. Qian, V. Rajaram, S. Kang, and M. Rinaldi, "NEMS infrared detectors based on high quality factor 50 nm thick AlN nano-plate resonators," in *2017 Joint Conference of the European Frequency and Time Forum and IEEE International Frequency Control Symposium (EFTF/IFCS)*, vol. 7. IEEE, jul 2017, pp. 500–501. [Online]. Available: http://ieeexplore.ieee.org/document/8088941/

[85] Y. Hui and M. Rinaldi, "Aluminum Nitride nano-plate infrared sensor with self-sustained CMOS oscillator for nano-watts range power detection," in *2013 Joint European Frequency and Time Forum & International Frequency Control Symposium (EFTF/IFC)*, no. 1. IEEE, jul 2013, pp. 62–65. [Online]. Available: http://ieeexplore.ieee.org/document/6702280/

[86] Z. Qian, S. Kang, V. Rajaram, and M. Rinaldi, "Narrowband MEMS resonant infrared detectors based on ultrathin perfect plasmonic absorbers," in *2016 IEEE SENSORS*. IEEE, oct 2016, pp. 1–3. [Online]. Available: http://ieeexplore.ieee.org/document/7808614/

[87] M. Rinaldi, C. Zuo, J. Van Der Spiegel, and G. Piazza, "Reconfigurable CMOS oscillator based on multifrequency AlN contour-mode MEMS resonators," *IEEE Transactions on Electron Devices*, 2011.